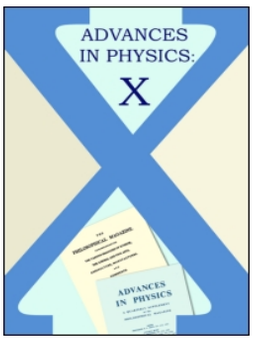

Advances in Physics: X

ISSN: (Print) 2374-6149 (Online) Journal homepage: https://www.tandfonline.com/loi/tapx20

Control of free electron wave packets by polarization-tailored ultrashort bichromatic laser fields

S. Kerbstadt, K. Eickhoff, T. Bayer & M. Wollenhaupt

To cite this article: S. Kerbstadt, K. Eickhoff, T. Bayer & M. Wollenhaupt (2019) Control of free electron wave packets by polarization-tailored ultrashort bichromatic laser fields, Advances in Physics: X, 4:1, 1672583, DOI: 10.1080/23746149.2019.1672583

To link to this article: https://doi.org/10.1080/23746149.2019.1672583

Published online: 23 Oct 2019.

ADVANCES IN PHYSICS: X
2019, VOL. 4, NO. 1, 1672583
https://doi.org/10.1080/23746149.2019.1672583

Taylor & Francis
Taylor & Francis Group

REVIEW ARTICLE

OPEN ACCESS Check for updates

Control of free electron wave packets by polarization-tailored ultrashort bichromatic laser fields

S. Kerbstadt, K. Eickhoff, T. Bayer and M. Wollenhaupt

Institut für Physik, Carl von Ossietzky Universität Oldenburg, Oldenburg, Germany

ABSTRACT

We review recent advances in the generation of polarization-tailored ultrashort bichromatic laser fields and their application to the coherent control of ultrafast photoionization dynamics. In the experiments, we use polarization-shaped bichromatic laser pulses to control three-dimensional photoelectron momentum distributions from atomic multiphoton ionization. To analyze the underlying physical mechanisms, we consider two bichromatic control schemes based on high-order intrapulse frequency mixing and interband N_1- vs. N_2-photon interference, respectively. In the first scheme, interferometric (ω:2ω) fields are used to select or suppress specific ionization channels in the resonance-enhanced 2-photon ionization of potassium atoms by second-order intrapulse frequency mixing. In the second scheme, we utilize a white light polarization pulse shaper to generate carrier-envelope phase-stable (3ω:4ω) fields in order to manipulate the symmetry properties of photoelectron wave packets from 3- vs. 4-photon ionization of sodium atoms. In both cases, bichromatic polarization control of free electron wave packets is based on the creation of a superposition of multiple angular momentum states with different kinetic energy spectra. We discuss the vorticity of these mixed angular momentum states and show that the kinetic energy spectra are determined by the bichromatic multiphoton spectra, emphasizing the close relationship between bichromatic multiphoton ionization and nonlinear optical spectroscopy.

ARTICLE HISTORY
Received 31 May 2019
Accepted 16 September 2019

KEYWORDS
Multiphoton ionization; coherent control; bichromatic fields; polarization pulse shaping; carrier-envelope phase control; photoelectron tomography; ultrafast dynamics

CONTACT M. Wollenhaupt Matthias.Wollenhaupt@uni-oldenburg.de Institut für Physik, Carl von Ossietzky Universität Oldenburg, Carl-von-Ossietzky-Straße 9–11, Oldenburg D-26129, Germany

Present address for S. Kerbstadt is Center for Free-Electron Laser Science (CFEL), Deutsches Elektronen-Synchrotron DESY, Hamburg, Germany.

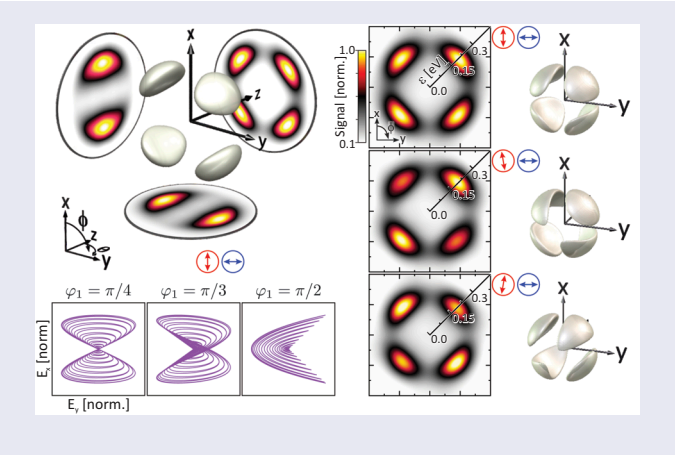

1. Introduction

The advent of femtosecond laser pulse sources has opened up the possibility to access atomic and molecular dynamics on their intrinsic ultrafast timescales. In particular, the design of tailored light fields to manipulate the interferences of matter waves was found to be the key for the coherent control of quantum phenomena. By this means, a quantum system can be driven from an initial state into a predefined target state, enabling far-reaching applications in the interdisciplinary field of femtosecond science [1–14]. The degree of control over the target state is constantly enhanced by the rapid progress of the laser techniques in the femto- [15–17] and the attosecond regime [18–22] covering a large range of tunable center wavelengths [16,17,23,24]. Novel pulse shaping techniques enable unprecedented control over the amplitude, phase and polarization of such ultrashort laser pulses [17,25–34].

In recent years, particularly bichromatic laser fields [35–38] have emerged as powerful twist in a variety of research fields, e.g. for the coherent control of electron dynamics in atoms [37,39–45], molecules [46–48] and solids [49–52]. Polarization-shaped bichromatic fields play an especially prominent role in the field of attosecond science [19–22,53,54] where such fields are routinely used for the control of high-harmonic generation (HHG) and the production of attosecond laser pulses. For example, linearly polarized bichromatic driving pulses are used for the generation of even harmonics [35,55–58] and tunable HHG radiation [59,60], shaping of the attosecond pulse train [61–64] and spectral focusing/efficiency enhancement of HHG [35,39,65,66]. Circularly polarized bichromatic driving pulses are employed for the production of elliptically polarized harmonics, as proposed in [35,36,57,67] and first demonstrated in [68–70]. In general, polarization-shaped bichromatic fields consist of two spectrally separated

bands with individually adjustable state of polarization. Depending on the polarization states, especially commensurable fields exhibit unusual polarization characteristics. Orthogonal linearly polarized (OLP) fields feature Lissajous-type polarization profiles, as illustrated in Figure 4(f). In contrast, co-rotating circularly polarized (COCP) fields have heart-shaped polarization profiles (see Figure 8(b)), whereas counter-rotating circularly polarized (CRCP) feature propeller-shaped profiles (see Figure 8(c)). The resulting even- or odd-numbered field symmetries are tunable by the center frequency ratio [71,72]. These symmetry properties of bichromatic fields were shown to have profound consequences on light-matter interactions [37,38] and give rise to unusual symmetries of matter waves. This was recently demonstrated in atomic strong-field ionization in both the multiphoton ionization (MPI) regime [71,73,74] and in the tunneling ionization regime [43,75,76]. In molecular HHG, the interplay between the symmetry of CRCP bichromatic driving fields and the symmetry of molecules has been investigated [77–79]. Bicircular HHG spectroscopy has been demonstrated as a tool to extract dynamical and spectroscopic information on atomic and molecular symmetries [77,78,80] and proposed as a technique to generate attosecond magnetic field pulses [81] for applications in ultrafast magneto-optics [72].

COCP and CRCP bichromatic fields were originally introduced in HHG to control the rescattering process of electrons from tunneling ionization recolliding with the parent ion [35,55,57]. For the bicircular case, Becker *et al.* found that HHG in atoms driven by commensurable CRCP fields is highly efficient as opposed to COCP fields [82]. This dependence of the recollision efficiency on the symmetry of the bicircular field was recognized even earlier [35,55,57] and confirmed recently [79,83]. It was shown that, when analyzed in a rotating frame [55,80,84], the electron experiences a linear acceleration, corresponding to a linearly polarized laser field, accompanied by a Coriolis-type deflection in perpendicular direction [81,83] counteracting the electron recollision. The influence of the deflection is larger for the COCP than for the CRCP case thus explaining the observed differences in HHG efficiency. For a recent review on highly nonlinear optical processes such as HHG, that are beyond the scope of this article, see for example [22]. In the following, we focus on perturbative multi-photon excitation and ionization dynamics of atoms in polarization-shaped bichromatic fields.

Sculpted free electron wave packets created by photoionization of atoms and molecules using tailored ultrashort laser pulses are currently studied by numerous groups in a variety of applications. For example, photoelectron momentum distributions (PMDs) with odd symmetries were created by atomic MPI [71] and strong-field ionization [43,75,76] using bichromatic CRCP fields. In addition, photoelectron and photoion momentum

distributions from nonsequential double ionization in (ω:2ω) CRCP [43,44] and OLP [85] fields have been investigated employing coincidence detection techniques [86]. The CEP-dependent directional photoemission from atoms in phase-stabilized few-cycle femtosecond laser pulses has been studied in the multiphoton [74,87,88] and above threshold [89] ionization regime. Moreover, CEP-control of ultrafast electron localization in molecules was observed in [90] employing photoelectron imaging techniques [91]. The creation of free electron vortices by MPI of atoms and molecules using time-delayed CRCP pulse sequences is a rapidly emerging research field. Free electron vortices have initially been studied theoretically in the XUV and attosecond time regime [92–96] and demonstrated recently using IR femtosecond pulses [97,98] and white light supercontinua [71,98]. The tomographic reconstruction [99,100] of designer free electron wave packets from atomic MPI with polarization-tailored femtosecond laser pulses was reported in [101]. Furthermore, the evolution of ultrafast spin-orbit [102,103] and Rydberg [74,104] wave packets has been observed by mapping the dynamics into the three-dimensional (3D) PMD from time-resolved resonance-enhanced MPI (REMPI) with ultrashort pump-probe pulse sequences. The interference of multiple photoelectron wave packets from different ionization pathways was utilized as a holographic technique to measure quantum mechanical phases for the reconstruction of wave functions [98,104–107]. In chiral molecules, asymmetries in the PMD along the laser-propagation direction due to the photoelectron circular dichroism have been analyzed in the multiphoton regime using circularly polarized UV femtosecond pulses [108–111] and in the single photon regime using elliptically polarized XUV pulses from HHG [111–113]. In general, time-resolved photoelectron spectroscopy is widely used in attosecond science, e.g. for the characterization of XUV attosecond pulse trains via reconstruction of attosecond beating by interference of two-photon transitions (RABBITT) [18] and for the direct measurement of femtosecond light fields via attosecond streaking techniques [114,115]. The prominent attoclock technique for the measurement of time delays in tunneling ionization is based on the coincidence detection of photoelectrons and -ions from attosecond angular streaking in an elliptically polarized IR driving field [116,117]. For further applications of ultrafast photoelectron spectroscopy in attosecond science, we refer the reader to the excellent recent review and perspective articles (see for example [21,22,54,118] and references therein).

The polarization control of N-photon ionization is achieved by generating and manipulating a superposition of multiple angular momentum states

$$\mathbf{\Psi}_N(\omega,\theta,\boldsymbol{\phi}) = i^N \sum_{k=0}^{N} \mathcal{S}_{N-k,k}(\omega)\, w_{N,N-2k}\, Y_{N,N-2k}(\theta,\boldsymbol{\phi}), \tag{1}$$

where $Y_{\ell,m}(\theta,\phi)$ denote the spherical harmonics and $w_{N,N-2k}$ take into account the relative transition strength of all paths leading to a final state $\mathcal{S}_{N-k,k}(\omega)Y_{N,N-2k}(\theta,\phi)$ (for details see Appendix). In the absence of intermediate resonances, the kinetic energy spectra corresponding to each angular momentum state are determined by the bichromatic Nth-order spectra $\mathcal{S}_{n_l,n_r}(\omega)$ defined in Equation (16) [119], emphasizing the close relationship between bichromatic MPI and nonlinear optical spectroscopy. The measured electron wave packet is determined by the coherent superposition of all interfering angular momentum states in the ionization continuum. If the optical phases of the driving pulses result in a relative quantum phase between the interfering electronic wave functions, phase control of the generated superposition states is attained. Depending on the optical parameters of the driving pulses, including the center frequencies $\omega_{1,2}$, the polarizations, the relative phases $\varphi_{1,2}$, the carrier-envelope phase φ_{ce} (CEP) and the time delay τ, control over the differential cross-section, for example, the angular distribution, and/or the integral cross-section, i.e. the photoelectron yield, is achieved [14].

In this contribution, we show that polarization-shaping of bichromatic fields allows a refined control of generated PMDs (i.e. along the polar angle (θ), the azimuthal angle (ϕ) and the kinetic energy ($\hbar\omega$)) via the interplay of spectral interference and quantum mechanical dipole selection rules for optical transitions. To this end, we study the two relevant control mechanisms in bichromatic MPI, as presented in Figure 1. The first mechanism

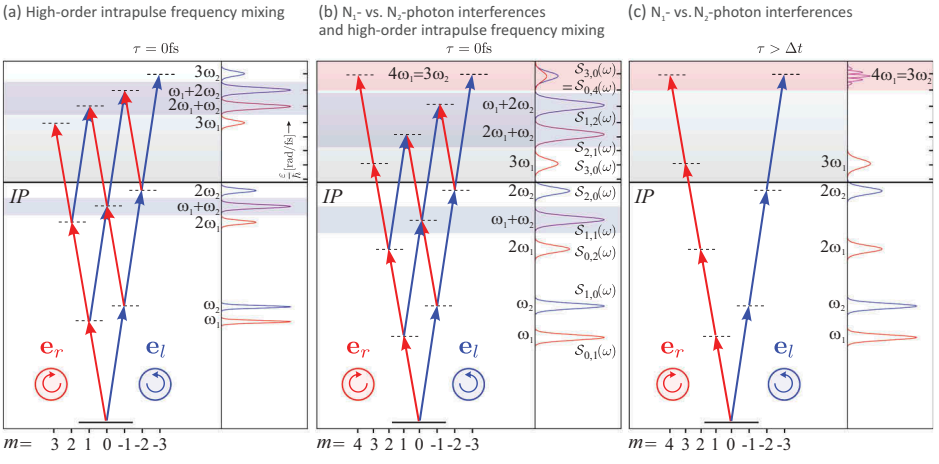

Figure 1. Ionization schemes for bichromatic MPI (*IP* is the ionization potential). (a) Third-order intrapulse frequency mixing from MPI with temporally overlapping ($\tau = 0$fs) incommensurable bichromatic fields. (b)–(c) MPI driven by temporally overlapping (3ω:4ω) fields. $\mathcal{S}_{n_l,n_r}(\omega)$ denotes the nonlinear spectra for the absorption of n_l LCP and n_r RCP photons. (c) N_1- vs. N_2-photon interferences persist when the pulses are temporally separated ($\tau > \Delta t$). Δt describes the pulse duration of the fields of both colors.

under investigation is based on high-order intrapulse frequency mixing of spectral bands with different ellipticities [73], while the second control mechanism is based on interband interferences between electronic wave functions coupled to the ground state by different numbers of photons, i.e. N_1- vs. N_2-photon interferences [71,74,97].

Specifically, bichromatic control by high-order intrapulse frequency mixing is based on the interference of electronic wave functions, which are excited by the absorption of N photons with different spectral bands and different ellipticities. In bichromatic N-photon ionization with two temporally overlapping ($\tau < \Delta t$) pulses, spectrally centered at ω_1 and ω_2, respectively, $(N-1)$ distinct contributions from frequency mixing arise in the photoelectron spectrum at $(N-k)\hbar\omega_1 + k\hbar\omega_2 - IP$, with $k = 1 \ldots (N-1)$. In Figure 1(a,b), kinetic energy spectra from bichromatic three-photon ionization are shown. In this case, third-order intrapulse frequency mixing from MPI with temporally overlapping incommensurable bichromatic fields leads to two energetically disentangled continuum states at $2\hbar\omega_1 + \hbar\omega_2 - IP$ and $\hbar\omega_1 + 2\hbar\omega_2 - IP$ (highlighted in light gray), as illustrated in Figure 1(a). These frequency mixing contributions are located between the single-color MPI signals at $3\hbar\omega_1 - IP$ and $3\hbar\omega_2 - IP$, which are generated solely by the individual colors. The frequency mixing process is very efficient due to the large number of pathways leading to the same final state. Frequency mixing is also robust, because PMDs are not affected by CEP fluctuations. Provided the spectral bands of the driving fields are disjointed, also the spectral phases $\varphi_{1,2}(\omega)$ of the driving fields, including the relative phases and additional spectral phase modulation functions, do not alter the photoelectron angular distribution. The latter is determined by the angular momentum states contributing to the coherent superposition in Equation (1). Which angular momentum target states are excited specifically, is determined by the polarization state of the laser pulse via the dipole selection rules for $\sigma^{\pm}$-transitions. Left-handed circularly polarized (LCP) laser pulses drive only σ^{+}-transitions, which increase the magnetic quantum number by $\Delta m = +1$, while right-handed circularly polarized (RCP) pulses drive σ^{-}-transitions decreasing the magnetic quantum number by $\Delta m = -1$. In addition, the orbital quantum number ℓ is either increased by $\Delta\ell = +1$ or decreased by $\Delta\ell = -1$. For simplicity, here we consider only $\Delta\ell = +1$ transitions, which are favored by propensity rules [120,121]. In an N-photon ionization scenario, single color LCP and RCP pulses hence excite a single angular momentum state with $|\ell, m\rangle = |N, +N\rangle$ and $|N, -N\rangle$, respectively. In a bichromatic CRCP pulse sequence, however, any state $|N, N-2k\rangle$ with $k = 0 \ldots N$ is accessible by mixing of LCP and RCP photons (cf. Equation (1)). Recently, background-free pump-probe spectroscopy exploiting the energetic disentanglement of the pump and probe

signals in bichromatic frequency mixing has been demonstrated [74,103]. In addition, the potential of polarization-shaped bichromatic fields to generate and manipulate angular momentum superposition states with unusual symmetry properties has been studied in [73].

While high-order intrapulse frequency mixing always occurs in bichromatic MPI with temporally overlapping fields, N_1- vs. N_2-photon interferences require bichromatic fields with specific commensurable center frequencies $\omega_2 = \frac{N_2}{N_1}\omega_1$. Then, overlapping photoelectron spectra at $\hbar N_1\omega_2 = \hbar N_2\omega_1$ enable interferences of continuum states addressed by quantum pathways assigned to different numbers of photons (N_1 and N_2)

$$\boldsymbol{\Psi}(\omega,\theta,\boldsymbol{\phi}) = \boldsymbol{\Psi}_{N_1}(\omega,\theta,\boldsymbol{\phi}) + \boldsymbol{\Psi}_{N_2}(\omega,\theta,\boldsymbol{\phi}). \tag{2}$$

These interband interferences between N_1- and N_2-photon quantum pathways are based on the superposition of electronic wave functions, which are individually controllable by the pulses within the driving sequence [14,74,87,122,123]. For interband interferences to occur, no mixing of different spectral bands is required. In this case, the polarization state of each color determines the angular momentum of the respective final state via $\boldsymbol{\Delta}m$-selection rules. The optical amplitude and phase of each color control the respective quantum mechanical amplitude and phase of the individual wave function. For this reason, the stability of both the CEP and the relative phases is crucial for the detection of interband interferences. In contrast to high-order intrapulse frequency mixing, interband interferences are observed independently of the temporal overlap of the pulses, as shown in Figure 1(b,c). At $\tau = 0$fs, the multiphoton spectrum is dominated by high-order intrapulse frequency mixing processes, which are more efficient than the interband interferences. Introducing a time delay $\tau > \boldsymbol{\Delta}t$ between the fields of both colors permits to prepare almost pure N_1- vs. N_2-photon interferences, because the contributions from high-order frequency mixing vanish. Figure 1(b,c) illustrate MPI by temporally overlapping and time-delayed (3ω:4ω) fields.

This article is structured as follows. In Section 2, we show that second-order intrapulse frequency mixing allows to selectively suppress and address predefined ionization channels. In these experiments, we generate polarization-shaped (ω:2ω) fields by nonlinear frequency conversion in a Mach–Zehnder interferometer. The use of (ω:2ω) OLP fields cancels the contribution of the $|d,0\rangle$- and $|s,0\rangle$-states. As a result, a fourfold rotationally symmetric photoelectron wave packet is observed. Changing the polarization from OLP to CRCP aligns the emitted photoelectrons parallel to the laser propagation axis by selectively addressing the superposition state $|d,0\rangle + |s,0\rangle$. To study interband interferences in Section 3.2, we generate

CEP-stable (3ω:4ω) pulses using our white light polarization pulse shaper [124,125]. Shaper-based first- and second-order optical cross-correlation techniques are used to characterize the bichromatic fields [74,124–129]. In photoionization experiments, we apply temporally overlapping COCP, CRCP, PLP and OLP (3ω:4ω) pulses to demonstrate full spatial control over CEP-sensitive photoemission. Bichromatic PLP fields are used to steer directional photoemission along the laser polarization, whereas COCP, CRCP and OLP fields are used to manipulate the symmetry properties of the generated free electron wave packets. Our results show that the bichromatic multiphoton spectra create a connection between bichromatic MPI and nonlinear optics. These spectra are the basis to describe the spectral characteristics of the light created by nonlinear parametric frequency conversion as well as the photoelectron wave packets created by MPI (cf. radial part in Equation (1)). In addition, we discuss our findings in the context of vortex states in optics and quantum physics. In Section 4, we summarize the main results and discuss future perspectives.

2. Intrapulse frequency mixing

In this section, we discuss second-order intrapulse frequency mixing in bichromatic 1 + 1 REMPI of potassium (K) atoms with (ω:2ω) fields. The ionization schemes for the perturbative interaction of CRCP and OLP (ω:2ω) fields are depicted in Figures 3(a) and 4(a), respectively. We use the CRCP scheme to demonstrate selective excitation of $|\ell, m = 0\rangle$-states, i.e. states with different angular momentum quantum numbers ℓ, but the same magnetic quantum number $m = 0$. In contrast, OLP fields create a superposition of angular momentum states $|\ell = 2, m\rangle$, having different magnetic quantum numbers $m = -2, 0, 2$, but the same $\ell = 2$. Using OLP pulses, we demonstrate the selective suppression of the ionization channels into the $|d, 0\rangle$- and $|s, 0\rangle$-states by destructive interference and manipulate the PMD in azimuthal (ϕ)-direction by tilting the linear polarization of one color, as shown in Figure 4(b–e). We start by describing the experimental setup in Section 2.1 and present the experimental results in Section 2.2.

2.1. Experimental scheme

The setup for the experiments on intrapulse frequency mixing, illustrated in Figure 2(a), consists of three main components: a commercial femtosecond laser system, an (ω:2ω) Mach–Zehnder interferometer [69] and a velocity map imaging (VMI) photoelectron spectrometer [91]. A CEP-stabilized *FEMTOLASERS* multipass chirped pulse amplifier (Rainbow 500 incl. CEP4 module, Femtopower HR 3kHz CEP, 0.8mJ pulse energy) provides 20fs-laser pulses centered at $\lambda_0 = 800$nm. (ω:2ω) fields are generated using

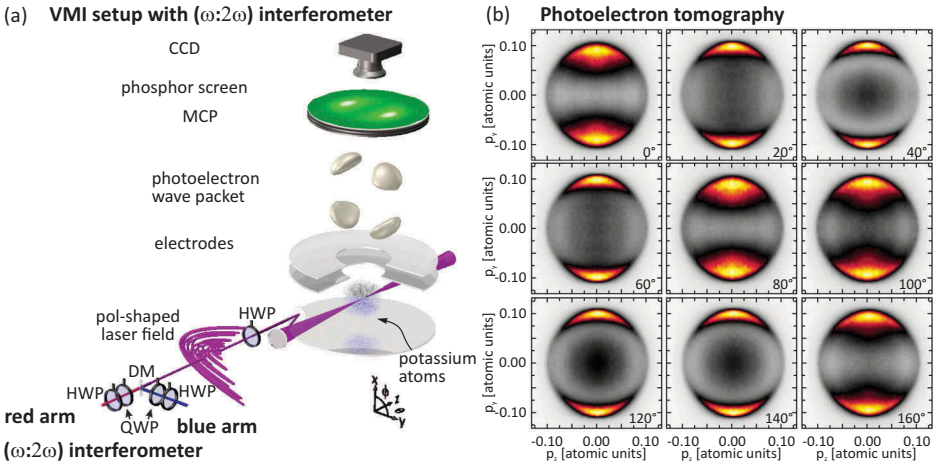

Figure 2. (a) Setup for VMI-based photoelectron tomography [99] for measurements of second-order intrapulse frequency mixing in the MPI of K atoms with (ω:2ω) fields. Polarization-shaped (ω:2ω) pulses are generated by a Mach–Zehnder interferometer equipped with quarter wave plates (QWPs) and half wave plates (HWPs). The fields are recombined with a dichroic mirror (DM) and focused with a spherical mirror (SFM) into the interaction region. For the photoelectron tomography, the pulses are rotated about the propagation axis with an additional HWP. Photoelectron wave packets created by MPI are projected onto a microchannel plate (MCP) detector followed by a phosphor screen and recorded by a charged coupled device (CCD) camera. (b) Selected projections generated by MPI with (ω:2ω) OLP fields. The photoelectron wave packets have a fourfold rotational symmetry, causing symmetrical projections.

an (ω:2ω) Mach–Zehnder interferometer, shown in Figure 2(a), to superimpose the fundamental amplifier beam (800nm) with its second harmonic (400nm). The second harmonic is created using a β-barium borate crystal. Each interferometer arm is equipped with a $\lambda/4$ plate and a $\lambda/2$ plate to generate either Lissajous-type OLP or propeller-type CRCP (ω:2ω) fields. The fundamental and its second harmonic are recombined using a dichroic mirror and then focused into the interaction region of the VMI spectrometer (peak intensity $I_0 \approx 2 \times 10^{12}\mathrm{W/cm^2}$) using a spherical focusing mirror with a focal length of $f = 250\mathrm{mm}$. VMI spectrometry allows us to detect angle- and energy-resolved top projections of the generated 3D PMDs from MPI of K atoms with polarization-tailored bichromatic pulses [71]. The interaction region is filled with K vapor supplied by a dispenser source (*SAES Getters*). The released photoelectrons are imaged onto a position-sensitive detector (*Scientific Instruments* S3075-10-I60-PS43-FM) consisting of a dual-layer micro-channel plate in chevron configuration followed by a phosphor screen. The two-dimensional (2D) projections are detected by a charge coupled device camera (*Lumenera* LW165M) using an exposure time of 250 ms. Each projection is acquired by the accumulation of 150 images. The 3D electron density is reconstructed using photoelectron

tomography [99,101]. For this purpose, the input pulse is rotated about the laser propagation axis by 180° with an angular step size of $\Delta\phi_{\lambda/2} = 4°$ using a superachromatic $\lambda/2$ plate (*Bernhard Halle Nachfl.*). Selected measured top projections are shown in Figure 2(b) for the OLP case. The 3D PMDs are retrieved from the projections using a Fourier-based tomographic algorithm [130].

2.2. Experimental results

Recently, the control of photoionization by third-order intrapulse frequency mixing was investigated [73]. Here, we reduce the photonic order of the process to study second-order intrapulse frequency mixing in 1 + 1 REMPI of K atoms using bichromatic (ω:2ω) fields. The results for CRCP and OLP fieds are presented in Secs. 2.2.1 and 2.2.2, respectively.

2.2.1. MPI with circularly polarized bichromatic fields (CRCP)

We start by discussing our results on second-order frequency mixing driven by (ω:2ω) CRCP fields. Due to the strong coupling of the states 4*s* and 4*p* by the resonant red pulse (800 nm), we consider only the ionization pathways depicted in Figure 3(a). After excitation of the 4*p*-state with the red right-handed circularly polarized (RCP) pulse, the blue left-handed circularly polarized (LCP) pulse ionizes the atoms to generate a coherent superposition of *s*- and *d*-type free electron wave packets with magnetic quantum

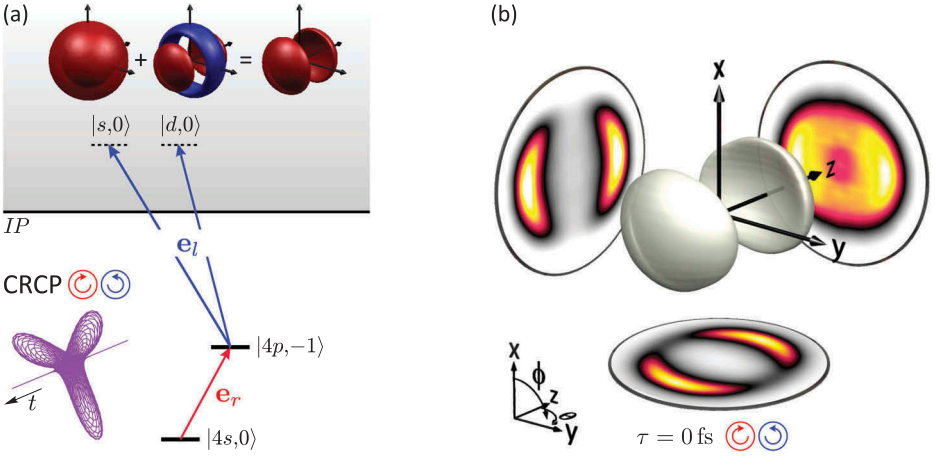

Figure 3. (a) Excitation scheme for second-order frequency mixing in the perturbative MPI of K atoms with (ω:2ω) CRCP fields. Two-photon CRCP ionization addresses $|d,0\rangle$- and $|s,0\rangle$-continuum states. The sign of the corresponding wave functions is color-coded. An (ω:2ω) CRCP propeller pulse is illustrated in the inset. (b) Tomographically reconstructed 3D photoelectron density. The PMD is aligned along the laser propagation direction due to the interference of the $|s,0\rangle$- and $|d,0\rangle$-wave packets.

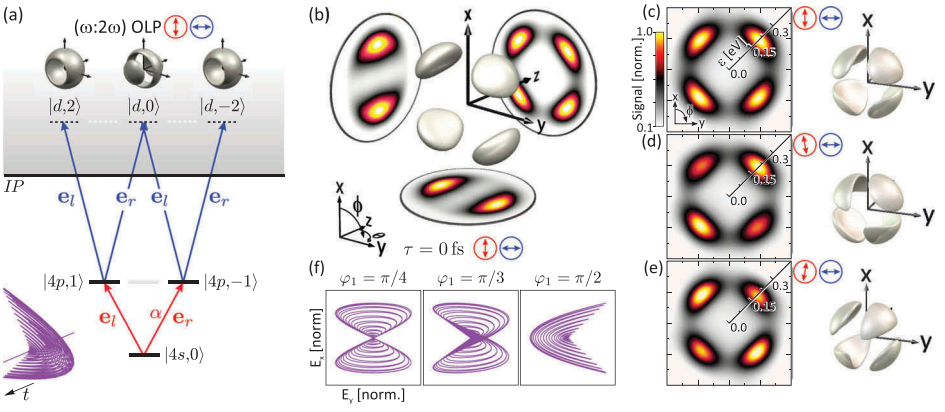

Figure 4. (a) Excitation scheme for second-order frequency mixing in the perturbative MPI of K atoms using (ω:2ω) OLP fields. The relative phase of $\alpha = \pi$ describes (ω:2ω) OLP fields in the circular basis. (b) Measured real-valued photoelectron wave packet $|d_{xy}\rangle = |d,2\rangle + |d,-2\rangle$ with c_4 rotational symmetry. (c)–(e) Measured x-y-sections taken through tomographically reconstructed photoelectron wave packets. Tilting the polarization of the red field leads to an inhomogeneity and a rotation in the azimuthal interference pattern, as shown in (d) and (e). Right: comparison to simulated 3D electron densities. (f) Polarization profiles of Lissajous-type (ω:2ω) OLP fields for different relative phases φ_1 between both colors.

number $m = 0$. Photoionization by three red photons is not taken into account, because the signal from the bichromatic 1 + 1 REMPI pathways turned out to be much more pronounced than the contribution from the single-color 1 + 2 REMPI. Since the relative phase between the fields of both colors was not stabilized, phase-sensitive asymmetries in the photoelectron spectra, as reported, for example, in [71,75,87,122,123], were not observed. Therefore, minor contributions of the three-photon ionization channel manifest – if at all – as weak symmetric offset which does not change the characteristics of the PMDs. The coherent superposition of the $|s,0\rangle$- and $|d,0\rangle$-states is strongly aligned along the laser propagation direction (z-axis) , as shown in Figure 3(b). Although it seems counterintuitive that the free electron wave packet is aligned perpendicularly to the polarization plane, this is a consequence of the selective excitation of $|\ell, m = 0\rangle$-states. The direct excitation of those states would require linearly polarized fields propagating in the x-direction with a polarization vector parallel to the z-direction. A similar electron wave packet alignment was recently observed due to the angular precession of spin-orbit wave packets from 1 + 2 REMPI in K atoms [103].

2.2.2. MPI with linearly polarized bichromatic fields (OLP)

In the second experiment, we vary the polarization state from CRCP to OLP by rotating the QWPs in both interferometer arms. In this scenario, second-order frequency mixing driven by (ω:2ω) OLP fields produces angular

momentum superposition states with different magnetic quantum numbers $m = -2, 0, 2$ and with the same orbital quantum number $\ell = 2$. The respective ionization scheme is illustrated in Figure 4(a). Following the arguments discussed in the CRCP case, we only consider the bichromatic 1 + 1 REMPI pathways depicted in Figure 4(a) in the following discussion. Now, we show that second-order frequency mixing by OLP fields cancels the population of the $|s, 0\rangle$- and $|d, 0\rangle$-continuum states via destructive interference. As illustrated in the excitation scheme in Figure 4(a), the vertical polarization of the red light field is described by the superposition of an LCP and a phase-shifted ($\alpha = \pi$) RCP field. The ionizing horizontally polarized blue field does not introduce further phases. As a consequence, the resonant field inflicts a relative quantum mechanical phase of π onto the ionization pathway $|4s, 0\rangle \rightarrow |4p, -1\rangle \rightarrow |d, 0\rangle$. Hence, both pathways $|4s, 0\rangle \rightarrow |4p, -1\rangle \rightarrow |d, 0\rangle$ and $|4s, 0\rangle \rightarrow |4p, 1\rangle \rightarrow |d, 0\rangle$ interfere destructively, leading to the cancellation of the population in the $|d, 0\rangle$-continuum state. The same argument applies to the $|s, 0\rangle$-continuum state. As a result, the electron wave packet is a superposition of two torus-shaped d-type continuum states, i.e. $|d, 2\rangle + |d, -2\rangle$ with no contribution from the $|d, 0\rangle$- and the $|s, 0\rangle$-states. This angular momentum superposition state is a realization of the real-valued $|d_{x,y}\rangle$-state, which exhibits a c_4 rotational symmetry, as shown in Figure 4(b). The generation of a real-valued superposition state $|\ell, \ell\rangle + |\ell, -\ell\rangle$ via complete destructive interference of all states $|\ell, m\rangle$ with $|m| \neq \ell$ is only achieved in this ionization scheme with $\ell = 2$. Recently, we have shown that third-order frequency mixing allows to generate photoelectron wave packets with quasi c_6 rotational symmetry [73]. In these experiments, residual contributions of $|f, \pm 1\rangle$-states did not cancel completely.

In the second-order frequency mixing scenario presented above, the relative optical phases between the ionizing bichromatic fields $E_{1,2}$ (see Appendix for the definition of the fields) do not affect the PMD. As pointed out in the introduction, absorption of $N - k$ photons with the frequency ω_1 and k photons with the frequency ω_2 gives rise to photoelectrons centered at $(N - k)\hbar\omega_1 + k\hbar\omega_2 - IP$, all of which have the same spectral phase of $(N - k)\varphi_1 + k\varphi_2$. Provided the bichromatic spectral bands of the fundamental are disjointed – which is the case in all our experiments – the higher-order spectra do not overlap, precluding interference and thus phase control. Although the polarization profiles of the bichromatic field changes significantly by variation of the relative optical phases $\varphi_{1,2}$, the PMDs remain unchanged. For example, propeller-type CRCP fields are rotated by the relative phase between the fields of both colors [71] and Lissajous-type OLP fields change the whole polarization profile significantly, as depicted in Figure 4(f). Instead of changing the relative phase in the fields $E_{1,2}$, we can change the

polarization state of one pulse to manipulate the relative phase α between the LCP and RCP components, as illustrated in Figure 4 and discussed in detail in the Appendix. To demonstrate the control by the polarization state of the red pulse, we rotate the $\lambda/2$ plate in the red interferometer arm by $\pm 5^{\circ}$. In this way, it is possible to control the relative quantum mechanical phase α between the ionization paths leading to the $|d,0\rangle$-state. By rotating the polarization of the red pulse from OLP towards PLP, we reduce the relative quantum mechanical phase α and thus the degree of destructive interference in the $|d,0\rangle$-state[1]. As a consequence, its amplitude increases continuously, resulting in an inhomogeneous intensity distribution of the four azimuthal lobes visible in the measured x-y-sections in Figure 4(c–e). In addition, the decrease of α reduces the relative quantum phase between the $|d,\pm 2\rangle$-states, which leads to the azimuthal rotation of the PMD. Optically, the decrease of α results in the rotation of the polarization from OLP towards PLP. Quantum mechanically, the decrease of α results in an increasing inhomogeneity and an azimuthal rotation such that the PMD continuously transforms from a homogeneous fourfold rotationally symmetric wave packet into a (rotated) $|d,0\rangle$-state aligned along the laser polarization. For MPI driven by a bichromatic field with tilted linear polarizations or with a PLP field, the $|s,0\rangle$-state needs to be taken into account as well [98,131,132]. The simulated 3D electron densities on the right side of Figure 4(c–e) are in good agreement with the experimental results.

In this section, we have demonstrated the use of (ω:2ω) fields in a second-order frequency mixing 1 + 1 REMPI scheme to create and control specific angular momentum superposition states. Bichromatic CRCP pulses have been employed to create the superposition state $|s,0\rangle+|d,0\rangle$, which is aligned parallel to the propagation direction of the laser field. In further experiments, those ionization channels were selectively suppressed by destructive interference using bichromatic OLP pulses. In this way, the superposition state $|d_{x,y}\rangle = |d,-2\rangle + |d,2\rangle$ was created and manipulated by tilting the linear polarization of the red pulse.

3. Interband N_1- vs. N_2-photon interference

In this section, we investigate bichromatic polarization control of the interference of free electron wave packets created by perturbative ionization with different numbers of photons, i.e. by N_1- vs. N_2-photon ionization. In intrapulse frequency mixing discussed in the previous Section 2, the temporal overlap ($\tau < \Delta t$) of the two colors in the bichromatic field is the prerequisite for the simultaneous absorption of photons from both fields. In contrast, the interference from N_1- vs. N_2-photon ionization requires a driving field with commensurable center frequencies $\omega_2 = \frac{N_2}{N_1}\omega_1$ to ensure

the energetic overlap of the nonlinear N_1th- and N_2th-order spectra. The interference of the continuum states from N_1- and N_2-photon ionization arises in an energy window centered around $\varepsilon = \hbar N_2\omega_1 - IP = \hbar N_1\omega_2 - IP$ and also remains for a time delay $\tau > \Delta t$ [71], as illustrated in Figure 1(b,c). Here, we implement a 3- vs. 4-photon interference scheme in the MPI of sodium (Na) atoms by temporally overlapping polarization-tailored (3ω:4ω) fields [71]. In contrast to high-order intrapulse frequency mixing, in this scheme, the relative optical phases $\varphi_{1,2}$ between the colors as well as the CEP φ_{ce} result in a relative quantum mechanical phase $\Delta\varphi$ (cf. Equation (4)) between the interfering electronic states. Therefore, in addition to the stability of the relative phases, also CEP stability is required to detect N_1- vs. N_2-photon interference patterns [74]. In the experiments, the bichromatic (3ω:4ω) fields are generated using a white light polarization pulse shaper equipped with a custom composite polarizer in the Fourier plane [124,125] (see Section 3.1). In addition to CEP control, we manipulate the photoelectron wave packets from 3- and 4-photon ionization by varying the bichromatic polarization state, employing circularly (COCP and CRCP) and linearly polarized (PLP and OLP) bichromatic (3ω:4ω) pulses. Our results reveal a 3D control of the symmetry properties of photoelectron wave packets generated by COCP, CRCP, and OLP (3ω:4ω) fields and controlled directional photoemission along the laser polarization using PLP fields.

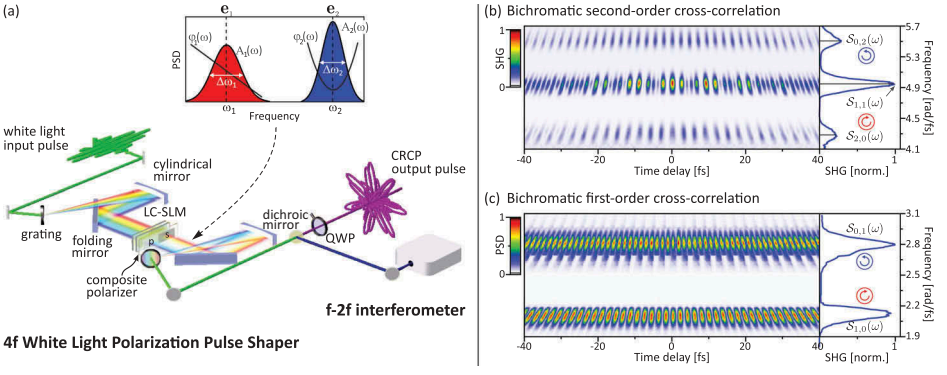

Figure 5. (a) Setup for the generation of polarization-tailored bichromatic laser fields using a composite polarizer in the Fourier plane of a 4*f* white light polarization pulse shaper, based on a liquid crystal spatial light modulator (LC-SLM). For the generation of circularly polarized fields, a quarter wave plate (QWP) is mounted at the shaper output. (b)–(c) Shaper-based pulse characterization by spectrally resolved cross-correlation traces of (3ω:4ω) CRCP fields, along with the corresponding spectra $\mathcal{S}_{n_l,n_r}(\omega)$ derived from the projections along the time axis. (b) The second-order cross-correlation trace has three distinct spectral peaks, two single-color contributions at $2\omega_{1,2}$ and a mixing contribution at $\omega_1 + \omega_2$. (c) The first-order cross-correlation trace has two maxima centered at $\omega_{1,2}$, respectively.

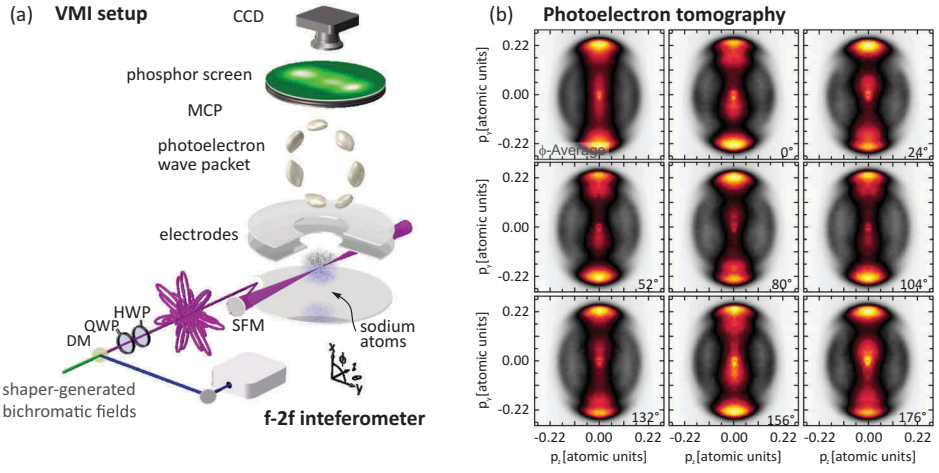

Figure 6. (a) Setup for photoelectron tomography based on VMI spectrometry. The polarization-shaped input pulse is focused into the interaction region filled with Na vapor using a spherical mirror (SFM). For the tomography, the shaped pulse is rotated about its propagation axis using a half wave plate (HWP). Projections of the wave packet are measured under different angles. The 3D density is retrieved from the projections using a Fourier-based reconstruction algorithm [99]. (b) Selected projections from MPI with CRCP fields measured under different angles. The projections exhibit a lateral asymmetry, which is inverted seven times as the pulse is rotated about π.

3.1. Experimental scheme

For the experiments, the above-mentioned femtosecond amplifier laser system (c.f. Section 2.1) is supplemented by a Neon-filled hollow-core fiber for white light supercontinuum generation [71,125], a 4*f* white light polarization pulse shaper (see Figure 5) and a home-built single-shot *f*-2*f* interferometer for active CEP control and stabilization [74]. The VMI spectrometer is used, in the same way as described above in Section 2.1, for angle- and energy-resolved photoelectron tomography [99] (see Figure 6). In the following, the setup for the N_1- vs. N_2-photon interference experiments is briefly described, a more detailed description is given in [71,74,125].

3.1.1. Bichromatic white light polarization shaping

In our experiments, polarization pulse shaping is based on a dual-layer liquid crystal spatial light modulator mounted in the Fourier plane of a 4*f* setup [28–34,133], allowing for either independent amplitude and phase or independent phase and polarization pulse shaping. However, a combination of both modes requires elaborate extensions of the 4*f* setup [134–140]. In addition, the adaption of 4*f* pulse shaping to ultra-broadband supercontinua [125,141,142], over-octave spanning spectra from molecular modulators [143,144] and frequency domain optical parametric amplification [145]

opens up exciting new perspectives for the generation of tailored intense laser pulses in the few-cycle regime with tunable center wavelengths [17]. To enable combined amplitude, phase and polarization pulse shaping tailored to the design of bichromatic fields, we recently introduced a shaper arrangement using a custom composite polarizer [124,125]. The composite polarizer, mounted directly behind the spatial light modulator, is divided in the spectral dimension into two parts with orthogonal transmission axes. With the composite polarizer, we sculpture a bichromatic amplitude profile from octave-spanning white light input pulses [125]. This approach provides full access to all bichromatic field parameters, as illustrated in the inset to Figure 5(a). For example, we can continuously tune the amplitude profiles $A_{1,2}(\omega)$ of both colors, including the center frequencies $\omega_{1,2}$, the amplitude ratio A_1/A_2, and the spectral bandwidths $\Delta\omega_{1,2}$. In addition, we can apply spectral phase functions $\varphi_{1,2}(\omega)$ to both colors individually. This enables us, in particular, to precisely adjust the relative phases $\varphi_{1,2}$ and a time delay τ between the two colors, as well as to control the CEP φ_{ce}. By choice of the polarizer (composite or conventional), the bichromatic polarization state can be selected between OLP and PLP. CRCP and COCP fields are generated by adjusting an additional superachromatic $\lambda/4$ plate at the shaper output [124,125]. To create the polarization-shaped (3ω:4ω) fields for the experiments, the center wavelengths are set to $\lambda_1 = 880\text{nm}$ and $\lambda_2 = 660\text{nm}$ and chosen such that 3- vs. 4-photon interferences arise around $\varepsilon \approx 0.5\text{eV}$ in the MPI spectra of Na atoms, as depicted in Figures 8(a) and 9(a). The peak intensity in the interaction region of the VMI was $I_0 \approx 2 \times 10^{12}\text{W/cm}^2$ corresponding to perturbative multiphoton excitation conditions.

In contrast to the (ω:2ω) fields created by the superposition of a fundamental laser beam and its second harmonic used in the experiments described in Section 2, the shaper-generated bichromatic fields are sensitive to both the relative phase $\varphi_{1,2}$ between the two colors and the CEP φ_{ce} [71,74]. The shaper-based approach allows us to generate a novel class of bichromatic waveforms, which permits us to combine bichromatic multipath interference schemes with CEP control and 4*f* shaping capabilities.

In addition, the setup serves as tool for pulse compression based on evolutionary optimization strategies [3,146] and for pulse characterization via shaper-based common-path cross-correlation measurements [74,124–126]. For shaper-based cross-correlation measurements of our two-color laser pulses presented in Figure 5(b), we adapted established techniques [126–129] to bichromatic fields. To this end, a bichromatic bandwidth-limited reference pulse is split off the phase-modulated bichromatic sample pulse via amplitude and phase modulation. By variation of the time delay between the sample and reference pulse, we detect either a linear feedback signal, e.g. the fundamental power spectral density, or a phase-sensitive

nonlinear signal, such as the second harmonic. Initially, we measure a bichromatic first-order cross-correlation trace by recording the power spectral density as a function of the time delay τ, as shown in Figure 5(c). Since the two field components are spectrally disjointed, we observe two distinct contributions centered at ω_1 and ω_2, respectively. In the CRCP case, depicted in Figure 5, the two optical peaks correspond to the first-order spectra $\mathcal{S}_{1,0}(\omega)$ and $\mathcal{S}_{0,1}(\omega)$ defined in Equation (16). The temporally- and spectrally-resolved cross-correlation map exhibits a delay-dependent spectral modulation of the individual bands, but does neither provide access to the pulse durations nor to the interference of the two colors. To characterize the shaper-generated bichromatic fields in time domain, we generate the second harmonic of the bichromatic field via nonlinear frequency conversion in a β-barium borate crystal and measure the temporal beating in the frequency mixing term at $\omega_1 + \omega_2$, as depicted in Figure 5(b). This second-order frequency mixing term, described by the nonlinear spectrum $\mathcal{S}_{1,1}(\omega)$, is analogous to high-order frequency mixing processes in quantum control experiments discussed in Section 2. The two signals at $2\omega_1$ and $2\omega_2$ are the optical counterparts of the single-color MPI contributions of only the red or the blue band, described by $\mathcal{S}_{2,0}(\omega)$ and $\mathcal{S}_{0,2}(\omega)$, respectively. Based on the shaper-based second-order cross-correlation traces, we extract information on the temporal profiles of the beating between the two colors and, in addition, on the pulse profiles of the two colors. However, the relative phases and the CEP cannot be extracted from the frequency mixing spectra, as discussed in Section 2.2.2. To achieve phase-sensitive interferences between the fields of both colors, spectrally overlapping nonlinear processes of different order are required, as discussed in detail in Section 3.2 on the example of 3- vs. 4-photon quantum pathway interferences in the MPI of Na atoms.

3.1.2. CEP stabilization

We use a home-built single-shot f-$2f$ interferometer for active CEP control and compensation of long-term CEP-drifts [74], as illustrated in Figures 5(a), 6(a). To ensure the ω-2ω overlap required for the CEP measurement, we sculpture an additional (ω:2ω) field from the wings of the octave-spanning white light input spectrum. This (ω:2ω) field is then split off the main beam by a dichroic mirror at the shaper output [71,74]. This procedure enables us to operate the f-$2f$ interferometer without further power loss in the spectral region relevant for the experiment. Furthermore, no additional spectral broadening of the f-$2f$ seed beam is required. The interferometer works on a single-shot basis with an acquisition rate of 85 Hz. At the same rate, the interferometer output directly feeds the active CEP control loop of the laser system, implemented by a piezo-controlled pair of wedges in the amplifier

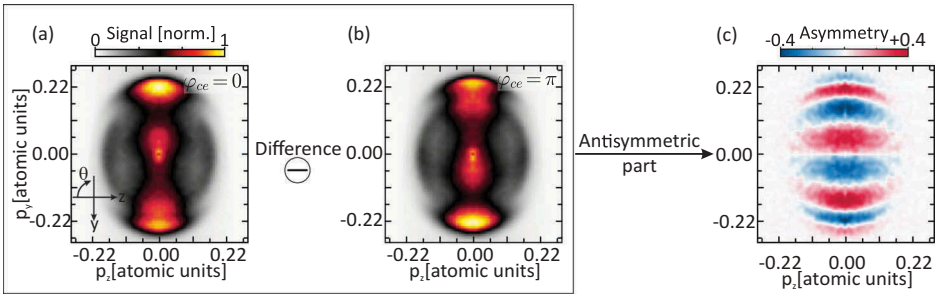

Figure 7. Illustration of the procedure for evaluating the CEP asymmetry contrast $\mathcal{A}(p,\theta)$ from the measured VMI images, as described by Equation (3). We calculate the difference of the measured photoelectron projections $\Delta\mathcal{P}(p,\theta) = \mathcal{P}(p,\theta;0) - \mathcal{P}(p,\theta;\pi)$ for a CEP of $\varphi_{ce} = 0$ (a) and $\varphi_{ce} = \pi$ (b). (c) The antisymmetric part of the difference $\Delta\mathcal{P}(p,\theta)$, i.e. the asymmetry contrast $\mathcal{A}(p,\theta)$ emphasizing the CEP-dependent features.

stage of the laser system, resulting in a long-term CEP stability of about 200 mrad root mean square measured over 3 h [71,74].

3.1.3. Evaluation of the cep-dependent asymmetry contrast in the VMI images

The VMI photoelectron spectrometer is described in Section 2.1 (see also Figure 6(a)). Again, we employ photoelectron tomography (cf. Section 2.1) to retrieve

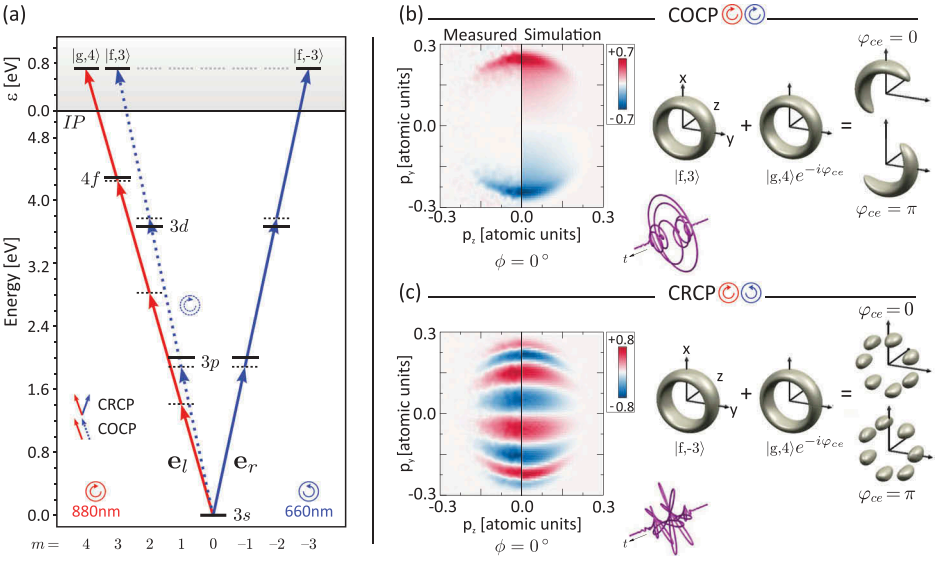

Figure 8. (a) Excitation scheme for the control of the CEP-sensitive photoemission from perturbative MPI of Na atoms using (3ω:4ω) COCP and CRCP fields. (b) COCP fields create a PMD in the shape of a crescent. (c) CRCP fields generate a standing wave pattern with seven azimuthal lobes. In both cases the driving bichromatic fields are sketched in the inset, along with simulated 3D photoelectron wave packets. The measured CEP-dependent asymmetry contrast $\mathcal{A}(p,\theta)$ (left) is compared to the simulation (right). The contributions from third-order frequency mixing are below the ionization potential of Na atoms ($IP = 5.13$eV).

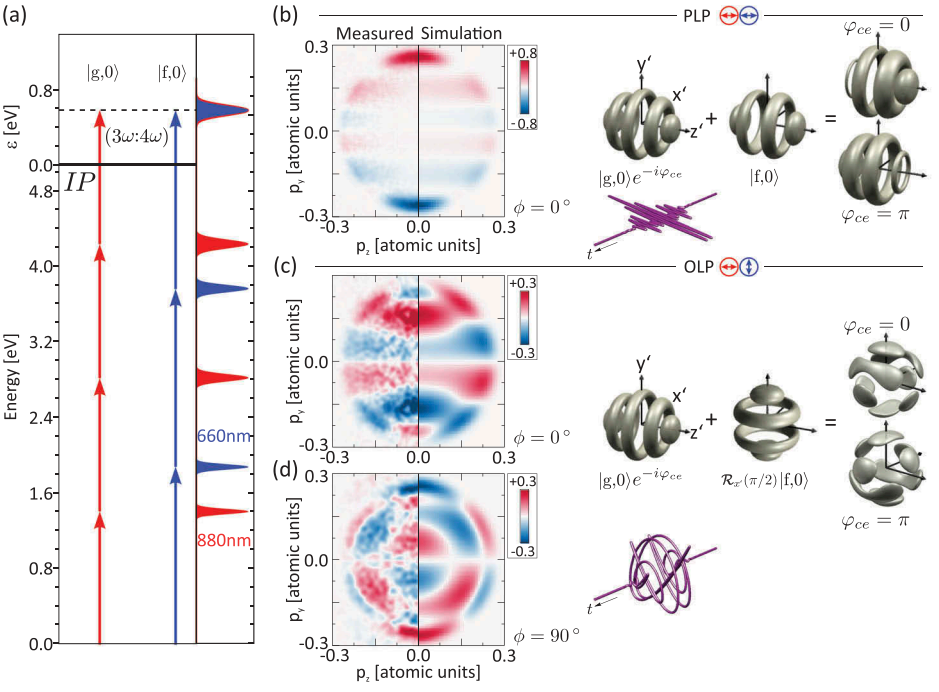

Figure 9. (a) Excitation scheme for CEP-sensitive photoelectron wave packets created by perturbative MPI of Na atoms with (3ω:4ω) PLP and OLP fields. (b) Control of the directional photoemission by bichromatic PLP laser fields. (c)–(d) OLP fields lead to a superposition of states with opposite parity and orthogonal symmetry axis. In both cases, the driving fields are sketched in the insets, along with simulated 3D photoelectron wave packets. The measured CEP-dependent asymmetry contrasts $\mathcal{A}(p,\theta)$ (left) are compared to simulations (right).

the 3D PMDs created by bichromatic MPI of Na atoms. To evaluate the CEP-sensitive asymmetry directly from the measured data, we recorded top projections $\mathcal{P}(p,\theta;\varphi_{ce})$ of the PMDs for $\varphi_{ce}=0$ and $\varphi_{ce}=\pi$, where p denotes the (transverse) momentum. Calculating the difference $\Delta\mathcal{P}(p,\theta)=\mathcal{P}(p,\theta;0)-\mathcal{P}(p,\theta;\pi)$ between both projections reveals the CEP-dependent features of the PMD. To enhance the visibility of the asymmetric features, we plot the anti-symmetric part $\mathcal{A}(p,\theta)$ of the difference $\Delta\mathcal{P}(p,\theta)$, as suggested in [74]

$$\mathcal{A}(p,\theta)=\frac{\Delta\mathcal{P}(p,\theta)-\Delta\mathcal{P}(p,-\theta)}{2}. \tag{3}$$

The procedure for deriving the asymmetry contrast $\mathcal{A}(p,\theta)$ is illustrated in Figure 7 on the data obtained by MPI of Na atoms with (3ω:4ω) CRCP fields. The asymmetry contrast shown in Figures 8 and 9 is evaluated with this method.

3.2. Experimental results

Shaper-generated bichromatic fields with low-order commensurable center frequencies are suitable tools to implement interband N_1- vs. N_2-photon interference schemes for manipulating symmetry properties of free electron wave packets from atomic MPI [14,71,74,103]. For example, bichromatic PLP pulse sequences have been used to control the directional photoemission in the MPI of xenon atoms by interband 7- vs. 8-photon interferences. The observed asymmetries in the PMD were caused by the interference of continuum states with opposite parity coupled to the ground state by quantum paths with a different number of photons. In the PLP case, the controllability of CEP-sensitive photoemission is essentially restricted to two distinct directions [74]. The full potential of bichromatic control of MPI has been exploited through the use of polarization-shaped bichromatic fields [43, 44, 71, 75]. Recently, interband 3- vs. 4-photon interferences have been observed in the CEP-sensitive photoemission from MPI of Na atoms using bichromatic (3ω:4ω) CRCP and COCP fields [71]. In that experiment, the generation and manipulation of matter waves with odd-numbered rotational symmetry has been demonstrated. Here, we discuss experimental results on the coherent control of the symmetry properties of PMDs from MPI of Na atoms using bichromatic (3ω:4ω) COCP and CRCP, PLP and OLP fields.

3.2.1. MPI with circularly polarized bichromatic fields (CRCP and COCP)

In the first part of the experiment, we use bichromatic (3ω:4ω) COCP and CRCP fields to investigate polarization control of interfering free electron wave packets from 3- vs. 4-photon ionization of Na atoms.

The corresponding excitation scheme is shown in Figure 8(a). The polarization profile of bichromatic COCP laser pulses is heart-shaped, as depicted in the inset to Figure 8(b). Due to the dipole selection rule $\Delta m = 1$ for the absorption of LCP light, MPI with COCP fields results in a coherent superposition of two corotating torus-shaped free electron wave packets

$$|\psi_{\mathrm{COCP}}\rangle \propto |f,3\rangle + i\,|g,4\rangle\, e^{-i\Delta\varphi}, \tag{4}$$

with the relative quantum phase $\Delta\varphi = 4\varphi_1 - 3\varphi_2 + \varphi_{ce}$ determined by the relative optical phases $\varphi_{1,2}$ and the CEP φ_{ce} of the driving fields [71]. In the discussion of the observed PMD, we focus on the azimuthal part of the wave function. Constructive interference in one hemisphere of the two torus-shaped wave packets and destructive interference in the other results in a crescent-shaped electron density, as visualized in the insets to Figure 8(b). The crescent-shaped PMD causes the emission of photoelectrons to be limited to one half of the laser polarization plane, the orientation of which is controlled by the optical phases.

Changing the CEP by $\Delta\varphi_{ce} = \pi$ rotates the laser pulse by an angle of π. The photoelectron wave packet is rotated by the same amount (see [71] for the derivation of the phase-dependent rotation of the bichromatic COCP and CRCP laser pulses and the corresponding electron wave packets). Due to this rotation, the photoelectron asymmetry is completely inverted. The complete inversion of the PMD manifests in the steep gradient in the y-direction observed in the measured asymmetry contrast $\mathcal{A}(p,\theta)$ shown in Figure 8(b). The experimental results are consistent with the simulation described by Equation (19) in the Appendix and depicted in the right part of Figure 8(b).

Now, we change the polarization state of the bichromatic field from COCP to CRCP [125]. The propeller-shaped polarization profile of a bichromatic CRCP pulse has seven propeller arms due to the frequency ratio of $\omega_2 = \frac{4}{3}\omega_1$, as shown in the inset to Figure 8(c). Photoionization with a bichromatic CRCP pulse creates a coherent superposition of two counter-rotating torus-shaped free electron wave packets

$$|\psi_{\text{CRCP}}\rangle \propto |f,-3\rangle + i|g,4\rangle\, e^{-i\Delta\varphi}, \tag{5}$$

as shown in the inserts to Figure 8(c). The superposition of the two counter-rotating angular momentum states gives rise to a spherical standing wave with seven azimuthal lobes, resulting in a free electron wave packet with c_7 rotational symmetry [71]. In contrast to the COCP case, the variation of the CEP by $\Delta\varphi_{ce} = \pi$ rotates the bichromatic CRCP laser polarization profile by only $\pi/7$. Correspondingly, the standing wave pattern of the free electron wave packet rotates half a cycle. The exchange of lobes and nodes in the PMD causes a pronounced oscillatory pattern in the measured asymmetry contrast $\mathcal{A}(p,\theta)$ in y-direction. This pattern is reproduced by the simulation shown in the right part of Figure 8(c).

3.2.2. MPI with linearly polarized bichromatic fields (PLP and OLP)

In the second part of the experiment, we investigate MPI with bichromatic PLP and OLP (3ω:4ω) fields. To simplify the notation for the angular momentum states when ionizing with linearly polarized fields, we change the coordinate system, as depicted in Figure 9(b–d). In this basis, electron wave packets from MPI with linearly polarized light along the z'-axis are no longer described by a superposition of states, but by a single $|\ell,0\rangle$-angular momentum state. Therefore, the photoelectron wave packet from ionization with bichromatic PLP fields is described by

$$|\psi_{\text{PLP}}\rangle \propto |f,0\rangle + i|g,0\rangle\, e^{-i\Delta\varphi}, \tag{6}$$

as shown in the insets to Figure 9(b). Because both partial waves in Equation (6) have opposite parity, their interference results in a phase-sensitive left-

right asymmetry of the PMD in the polarization plane. This asymmetry is inverted by altering the CEP by $\Delta\varphi_{ce} = \pi$. The measured and simulated asymmetry contrasts shown in Figure 9(b) are in good agreement. While PLP fields create superpositions of angular momentum states $|\ell, 0\rangle$ with different parity but same orientation, OLP pulses result in the coherent superposition of orthogonally oriented opposite parity states. Using the rotation operator $\mathcal{R}_{x'}(\phi)$ to describe a rotation about the x'-axis by an angle of ϕ, the angular momentum superposition state from MPI with bichromatic OLP fields reads

$$|\psi_{\mathrm{OLP}}\rangle \propto \mathcal{R}_{x'}(\pi/2)\,|f, 0\rangle + i|g, 0\rangle\, e^{-i\Delta\varphi}. \tag{7}$$

Due to the orthogonal symmetry axes of the involved angular momentum states, the resulting free electron wave packet has a very uncommon shape, which is controlled by the CEP, as illustrated in the insets to Figures 9(c,d). The asymmetry contrast $\mathcal{A}(p, \theta)$ in the projections measured under two different angles $\phi = 0°$ (y'-direction) and $\phi = 90°$ (z'-direction) also shows a complex modulation pattern, revealing the CEP-dependent features of the PMD. These results demonstrate the high degree of coherence and controllability of interfering matter waves from PLP and OLP bichromatic MPI involving different numbers of photons.

3.2.3. Vorticity analysis

So far, we have discussed two control schemes for the creation of angular momentum superposition states by atomic MPI using polarization-tailored bichromatic fields. Mixed orbital angular momentum states are of great interest in optics [147] and electron diffraction [148,149], because they are so-called vortex states. These states, characterized by a non-zero azimuthal probability density current and a helical phase front, play a prominent role in quantum mechanics [148,149]. In recent years, the fundamentals and applications of electron and optical vortex beams have been investigated extensively, both in theory and experiment [148,150]. For example, it has been shown that optical vortex beams produce high harmonics with tailored spin and orbital angular momenta, thus creating vortex beams in the extreme ultraviolet regime [151–153] and having a high potential for studies of chiral molecules [148,154,155]. Vortex states are characterized by a dimensionless winding number (vorticity) defined by [148]

$$l = \frac{1}{2\pi} \oint_{\mathcal{C}} \nabla \arg[\psi(r)] \cdot dr. \tag{8}$$

To calculate the vorticity l of the angular momentum superposition states generated by N_1- vs. N_2-photon ionization presented in Section 3.2, we derive the probability density current $j(r)$

$$j(r) \propto \Im[\psi^*(r)\nabla\psi(r)] = |\psi(r)|^2\nabla \arg[\psi(r)] = \frac{1}{2}|\psi(r)|^2\left(\frac{\tau}{\hbar}e_\varepsilon + \frac{(m_1+m_2)}{\varepsilon\sin(\theta)}e_\phi\right). \quad (9)$$

Herein, m_1 and m_2 denote the magnetic quantum numbers of the involved continuum states. For MPI with PLP bichromatic ($N_1\omega$:$N_2\omega$) fields, both m_1 and m_2 are zero. Therefore, the probability density current $j(r)$ has only components in radial direction and the vorticity vanishes, i.e. $l = 0$. The same holds for the single-color ($N_1 = N_2$) CRCP case, where $m_1 = -m_2$ [97]. The vorticity of the electron wave packets from MPI with circularly polarized ($N_1\omega$:$N_2\omega$) fields is most interesting. In this case, the magnetic quantum numbers m_1 and m_2 are directly given by the respective number of circularly polarized photons, i.e. by N_1 and N_2. Equation (9) shows that angular momentum superposition states from MPI with circularly polarized ($N_1\omega$:$N_2\omega$) fields have a non-vanishing azimuthal component of the probability density current $j(r)$, leading to a vorticity of

$$l = \frac{N_1 \pm N_2}{2}, \quad (10)$$

where the plus (minus) sign holds for bichromatic COCP (CRCP) fields. Considering $N_1 = 3$ and $N_2 = 4$, as used in the experiment, we obtain a fractional vorticity of $l = \frac{7}{2}$ for (3ω:4ω) COCP and $l = \frac{1}{2}$ for CRCP fields. This analysis shows that the creation of angular momentum superposition states by MPI with ($N_1\omega$:$N_2\omega$) fields is closely related to the concept of mixed orbital angular momentum states by superimposing multiple electron or optical vortex beams with different vorticities l [147–149].

4. Conclusion and outlook

In this article, we reported on recent advances in the generation of continuously tunable bichromatic polarization-tailored ultrashort laser pulses and their application for the coherent multipath control of atomic MPI. We investigated bichromatic MPI on quasi-single electron model systems (alkali atoms) to extract the physical mechanisms underlying phase- and polarization control. Our analysis revealed that the interplay of high-order intrapulse frequency mixing [73] and N_1- vs. N_2-photon interband interferences [71,74] is the key to coherent control of bichromatic MPI. The physical mechanism underlying both bichromatic control schemes, i.e. high-order intrapulse frequency mixing and N_1- vs. N_2-photon interband interferences,

is based on the creation of the superposition of multiple angular momentum states with different kinetic energy spectra. The photoelectron angular momentum superposition states with non-zero vorticity are analogous to vortex states discussed in optics and electron diffraction. The kinetic energy spectra, determined by the bichromatic multiphoton spectra, emphasize the close relationship between bichromatic MPI and nonlinear optical spectroscopy. In the experiments, both bichromatic control schemes were investigated individually. To this end, we used two approaches for the generation of polarization-shaped bichromatic fields. To demonstrate high-order intrapulse frequency mixing, we implemented an (ω:2ω) interferometer to superimpose the fundamental (800 nm) laser beam with its second harmonic (400 nm). A white light polarization pulse shaper equipped with a composite polarizer to generate polarization-controlled CEP-stable (3ω:4ω) fields was used to investigate N_1- vs. N_2-photon interband interferences.

In the experiments presented in Section 2.2, we studied second-order intrapulse frequency mixing in the 1 + 1 REMPI of K atoms driven by (ω:2ω) CRCP and OLP fields. Control by second-order frequency mixing allowed us to completely suppress or selectively address specific ionization pathways. Using bichromatic CRCP fields, we created the $|s,0\rangle + |d,0\rangle$-angular momentum superposition state, which is aligned along the laser propagation direction. In contrast, the real-valued angular momentum superposition state $|d_{xy}\rangle = |d,2\rangle + |d,-2\rangle$ with a c_4 rotational symmetry in the laser polarization plane was generated by ionization with bichromatic (ω:2ω) OLP fields.

CEP-sensitive 3- vs. 4-photon interband interferences in the MPI of Na atoms using shaper-generated (3ω:4ω) COCP, CRCP, PLP and OLP fields have been studied in the experiments presented in Section 3.2. MPI with polarization-tailored (3ω:4ω) fields was shown to enable full control over the symmetry properties of the generated PMDs. The CRCP fields allowed us to create a photoelectron wave packet with CEP-sensitive sevenfold rotational symmetry in the laser polarization plane [71]. In contrast, MPI with COCP fields localized the emitted photoelectrons in one half of the laser polarization plane by producing a PMD in the shape of a crescent. A fractional vorticity of $\frac{7}{2}$ and $\frac{1}{2}$ was calculated for the electron wave packets from ionization with bichromatic (3ω:4ω) COCP and CRCP fields, respectively. Using bichromatic PLP and OLP fields, we were able to control the directional photoemission along the laser polarization axis (PLP case) and to observe asymmetric PMDs by the interference of angular momentum states with opposite parities and with orthogonal symmetry axes (OLP case). The results showed the high degree of coherence of the free electron wave packets from MPI by absorption of different numbers of photons with

different colors and different polarization states. The coherence persisted even for MPI with bichromatic OLP pulses when continuum states with opposite parity and orthogonal symmetry axis interfere.

In the future, our experimental studies will be extended towards even more refined control schemes and more complex quantum systems including atomic and molecular multi-electron systems. The occurrence of electron-electron correlations and the coupling of multiple angular momenta alter the number and symmetry of intermediate states. This gives rise to additional resonances and bound state dynamics which may leave a fingerprint in the shape of the created free electron wave packets. In molecular systems, we plan to investigate the influence of the additional nuclear degrees of freedom on the PMD. While decoherence will play only a minor role on sufficiently short time scales, the rovibrational dynamics are expected to have a strong influence on the MPI processes. Using molecular alignment techniques, we will investigate how the nuclear configuration is imprinted in the shape of the PMD. Also de- and rephasing effects due to the propagation of vibrational wave packets are of fundamental interest, especially in time-delayed bichromatic excitation and ionization scenarios. By increasing the laser intensity and by varying the excitation wavelengths, we will study the transition from the multiphoton regime to the tunnel ionization regime. In particular, we are interested in the evolution of the symmetry properties of the polarization profile and the free electron wave packets as the intensity increases. Multi-color and multi-polarization laser pulse sequences will open up novel experimental techniques such as CEP- and polarization-sensitive background-free pump-probe experiments, quantum phase measurements and multi-dimensional spectroscopy approaches.

Notes

1. This argument applies also for the $|s, 0\rangle$ state.
2. For simplicity, only the $\Delta\ell = 1$ transitions have been considered here. In general, all paths with $\Delta\ell = \pm 1$ contribute to the final photoelectron momentum distribution as discussed in [98,156] and shown in Section2.2.

Disclosure statement

No potential conflict of interest was reported by the authors.

Funding

Financial support by the Deutsche Forschungsgemeinschaft via the DFG Priority Programme SPP 1840 QUTIF is gratefully acknowledged; Deutsche Forschungsgemeinschaft [Priority Programme SPP 1840 QUTIF].

References

[1] Judson RS, Rabitz H. Teaching lasers to control molecules. Phys Rev Lett. 1992;68:1500–1503.
[2] Zewail AH. Femtochemistry-ultrafast dynamics of the chemical bond I and II. New Jersey, Singapore: World Scientific; 1994.
[3] Baumert T, Brixner T, Seyfried V, et al. Femtosecond pulse shaping by an evolutionary algorithm with feedback. Appl Phys B. 1997;65:779–782.
[4] Meshulach D, Yelin D, Silberberg Y. Adaptive ultrashort pulse compression and shaping. Opt Commun. 1997;138:345–348.
[5] Rice SA, Zhao M. Optical control of molecular dynamics. New York, NYss: Wiley; 2000.
[6] Rabitz H, de Vivie-Riedle R, Motzkus M, et al. Whither the future of controlling quantum phenomena? Science. 2000;288:824–828.
[7] Levis RJ, Rabitz HA. Closing the Loop on Bond Selective Chemistry Using Tailored Strong Field Laser Pulses J. Phys Chem A. 2002;106:6427–6444.
[8] Wollenhaupt M, Assion A, Liese D, et al. Interferences of ultrashort free electron wave packets. Phys Rev Lett. 2002;89:173001.
[9] Tannor D. Introduction to quantum mechanics: a time-dependent perspective. Sausalito: University Science Books; 2007.
[10] Silberberg Y. Quantum coherent control for nonlinear spectroscopy and microscopy. Annu Rev Phys Chem. 2009;60:277–292.
[11] Ohmori K. Wave-packet and coherent control dynamics. Annu Rev Phys Chem. 2009;60:487–511.
[12] Fielding HH, Robb MA. Quantum molecular dynamics and control. Phys Chem Chem Phys. 2010;12:15569.
[13] Wollenhaupt M, Baumert T. Ultrafast laser control of electron dynamics in atoms, molecules and solids. Faraday Discuss. 2011;153:9–26.
[14] Shapiro M, Brumer P. Quantum control of molecular processes. 2nd ed. New York: Wiley; 2012.
[15] Brabec T, Krausz F. Intense few-cycle laser fields: frontiers of nonlinear optics. Rev Mod Phys. 2000;72:545–591.
[16] Cerullo G, Baltuska A, Mucke OD, et al. Few-optical-cycle light pulses with passive carrier-envelope phase stabilization. Laser Photonics Rev. 2011;5:323–351.
[17] Manzoni C, Mücke OD, Cirmi G, et al. Coherent pulse synthesis: towards sub-cycle optical waveforms. Laser Photonics Rev. 2015;9:129–171.
[18] Paul PM, Toma ES, Breger P, et al. Ultrafast lasers. Strobe light breaks the attosecond barrier. Science. 2001;292:1689–1692.
[19] Kling MF, Vrakking MJJ. Attosecond electron dynamics. Annu Rev Phys Chem. 2008;59:463–499.
[20] Krausz F, Ivanov M. Attosecond physics. Rev Mod Phys. 2009;81:163–234.
[21] Gallmann L, Cirelli C, Keller U. Attosecond science: recent highlights and future trends. Annu Rev Phys Chem. 2012;63:447–469.
[22] Calegari F, Sansone G, Stagira S, et al. Advances in attosecond science. Phys B. 2016;49:062001.
[23] Cerullo G, De Silvestri S. Ultrafast optical parametric amplifiers. Rev Sci Instrum. 2003;74:1–18.
[24] Grupp A, Budweg A, Fischer MP, et al. Broadly tunable ultrafast pump-probe system operating at multi-kHz repetition rate. J Opt. 2017;20:014005.
[25] Fermann ME, Da Silva V, Smith DA, et al. Shaping of ultrashort optical pulses by using an integrated acousto-optic tunable filter. Opt Lett. 1993;18:1505–1507.

[26] Dorrer C, Salin F, Verluise F, et al. Programmable phase control of femtosecond pulses by use of a nonpixelated spatial light modulator. Opt Lett. 1998;23:709–711.
[27] Verluise F, Laude V, Cheng Z, et al. Amplitude and phase control of ultrashort pulses by use of an acousto-optic programmable dispersive filter: pulse compression and shaping. Opt Lett. 2000;25:575–577.
[28] Weiner AM. Femtosecond pulse shaping using spatial light modulators. Rev Sci Instrum. 2000;71:1929–1960.
[29] Brixner T, Gerber G. Femtosecond polarization pulse shaping. Opt Lett. 2001;26:557–559.
[30] Präkelt A, Wollenhaupt M, Assion A, et al. Compact, robust, and flexible setup for femtosecond pulse shaping. Rev Sci Instrum. 2003;74:4950–4953.
[31] Brixner T, Krampert G, Pfeifer T, et al. Quantum control by ultrafast polarization shaping. Phys Rev Lett. 2004;92:208301.
[32] Wollenhaupt M, Krug M, Köhler J, et al. Photoelectron angular distributions from strong-field coherent electronic excitation. Appl Phys B. 2009;95:245–259.
[33] Wollenhaupt M, Bayer T, Baumert T. Control of ultrafast electron dynamics with shaped femtosecond laser pulses: From atoms to solids. In: Kitzler M., Gräfe S. (eds) Ultrafast Dynamics Driven by Intense Light Pulses. Springer Series on Atomic, Optical, and Plasma Physics, vol 86. Springer, Cham 2016.
[34] Misawa K. Applications of polarization-shaped femtosecond laser pulses Adv Phys X. 2016;1:544–569.
[35] Eichmann H, Egbert A, Nolte S, et al. Polarization-dependent high-order two-color mixing. Phys Rev A. 1995;51:R3414–R3417.
[36] Milosevic DB, Becker W, Kopold R. Generation of circularly polarized high-order harmonics by two-color coplanar field mixing. Phys Rev A. 2000;61:063403.
[37] Ehlotzky F. Atomic phenomena in bichromatic laser fields. Phys Rep. 2001;345:176–264.
[38] Ivanov M, Pisanty E. Taking control of polarization. Nat Photonics. 2014;8:501–503.
[39] Watanabe S, Kondo K, Nabekawa Y, et al. First experimental limit on the 19Ne(p, gamma)20Na resonance strength, of astrophysical interest. Phys Rev Lett. 1994;73:2692–2695.
[40] Kitzler M, Lezius M. Spatial control of recollision wave packets with attosecond precision. Phys Rev Lett. 2005;95:253001.
[41] Brugnera L, Hoffmann DJ, Siegel T, et al. Trajectory selection in high harmonic generation by controlling the phase between orthogonal two-color fields. Phys Rev Lett. 2011;107:153902.
[42] Xie XH, Roither S, Gräfe S, et al. Probing the influence of the Coulomb field on atomic ionization by sculpted two-color laser fields. New J Phys. 2013;15:043050.
[43] Eckart S, Richter M, Kunitski M, et al. Nonsequential double ionization by counter-rotating circularly polarized two-color laser fields. Phys Rev Lett. 2016;117:133202.
[44] Mancuso CA, Dorney KM, Hickstein DD, et al. Controlling nonsequential double ionization in two-color circularly polarized femtosecond laser fields. Phys Rev Lett. 2016;117:133201.
[45] Hasovi E, Becker W, Miloševi DB. Cavity-enhanced eigenmode and angular hybrid multiplexing in holographic data storage systems. Opt Express. 2016;24:6413–6424.
[46] Sheehy B, Walker B, DiMauro LF. Linearly positive histories: probabilities for a robust family of sequences of quantum events. Phys Rev Lett. 1995;74:4799–4802.
[47] Ohmura H, Saito N, Tachiya M. Selective ionization of oriented nonpolar molecules with asymmetric structure by phase-controlled two-color laser fields Phys Rev Lett. 2006;96:173001–173001–4.

[48] Ray D, He F, De S, et al. Ion-energy dependence of asymmetric dissociation of D 2 by a two-color laser field. Phys Rev Lett. 2009;103:223201.
[49] Dupont E, Corkum PB, Liu HC, et al. Linearly positive histories: probabilities for a robust family of sequences of quantum events. Phys Rev Lett. 1995;74:3596–3599.
[50] Hübner J, Rühle WW, Klude M, et al. Field fluctuation spectroscopy in a reverberant cavity with moving scatterers. Phys Rev Lett. 2003;90:216601.
[51] Costa L, Betz M, Spasenovic M, et al. All-optical injection of ballistic electrical currents in unbiased silicon. Nat Phys. 2007;3:632–635.
[52] Güdde J, Rohleder M, Meier T, et al. The Chlamydomonas genome reveals the evolution of key animal and plant functions. Science. 2007;318:1287–1291.
[53] Corkum PB, Krausz F. Attosecond science. Nat Phys. 2007;3:381–387.
[54] Vrakking MJJ. Attosecond imaging. Phys Chem Chem Phys. 2014;16:2775.
[55] Zuo T, Bandrauk ADJ. High-order harmonic generation in intense laser and magnetic fields. Nonlin Opt Phys Mater. 1995;04:533–546.
[56] Perry MD, Crane JK. High-order harmonic emission from mixed fields. Phys Rev A. 1993;48:R4051–R4054.
[57] Long S, Becker W, McIver JK. Model calculations of polarization-dependent two-color high-harmonic generation. Phys Rev A. 1995;52:2262–2278.
[58] Dudovich N, Smirnova O, Levesque J, et al. Measuring and controlling the birth of attosecond XUV pulses. Nat Phys. 2006;2:781–786.
[59] Eichmann H, Meyer S, Riepl K, et al. Generation of short-pulse tunable XUV radiation by high-order frequency mixing. Phys Rev A. 1994;50:R2834–R2836.
[60] Gaarde MB, Antoine P, Persson A, et al. High-order tunable sum and difference frequency mixing in the XUV region. Phys B. 1996;29:L163–L168.
[61] Corkum PB, Burnett NH, Ivanov MY. Error correction for increasing the usable capacity of photorefractive memories. Opt Lett. 1994;19:1870–1872.
[62] Ivanov M, Corkum PB, Zuo T, et al. Linearly positive histories: probabilities for a robust family of sequences of quantum events. Phys Rev Lett. 1995;74:2933–2936.
[63] Oishi Y, Kaku M, Suda A, et al. Generation of extreme ultraviolet continuum radiation driven by a sub-10-fs two-color field Opt Express. 2006;14:7230–7237.
[64] Mauritsson J, Dahlstrom JM, Mansten E, et al. Sub-cycle control of attosecond pulse generation using two-colour laser fields. Phys B. 2009;42:134003.
[65] Kim IJ, Kim CM, Kim HT, et al. Smearing of phase transition due to a surface effect or a bulk inhomogeneity in ferroelectric nanostructures. Phys Rev Lett. 2005;94:243901.
[66] Raz O, Pedatzur O, Bruner BD, et al. Spectral caustics in attosecond science. Nat Photonics. 2012;6:170–173.
[67] Milosevic DB, Becker W. Attosecond pulse trains with unusual nonlinear polarization. Phys Rev A. 2000;62:011403R.
[68] Fleischer A, Kfir O, Diskin T, et al. Spin angular momentum and tunable polarization in high-harmonic generation. Nat Photonics. 2014;8:543–549.
[69] Kfir O, Grychtol P, Turgut E, et al. Generation of bright phase-matched circularly-polarized extreme ultraviolet high harmonics. Nat Photonics. 2015;9:99–105.
[70] Fan TT, Grychtol P, Knut R, et al. Bright circularly polarized soft X-ray high harmonics for X-ray magnetic circular dichroism. PNAS. 2015;112:14206–14211.
[71] Kerbstadt S, Eickhoff K, Bayer T, et al. Odd electron wave packets from cycloidal ultrashort laser fields. Nat Commun. 2019;10:658.
[72] Bandrauk AD, Guo J, Yuan KJ. Circularly polarized attosecond pulse generation and applications to ultrafast magnetism. J Opt. 2017;19:124016.

[73] Kerbstadt S, Pengel D, Johannmeyer D, et al. Control of photoelectron momentum distributions by bichromatic polarization-shaped laser fields. New J Phys. 2017;19:103017.
[74] Kerbstadt S, Pengel D, Englert L, et al. Carrier-envelope-phase control of asymmetries in the multiphoton ionization of xenon atoms by ultrashort bichromatic fields. Phys Rev A. 2018;97:063402.
[75] Mancuso CA, Hickstein DD, Grychtol P, et al. Strong-field ionization with two-color circularly polarized laser fields. Phys Rev A. 2015;91:031402R.
[76] Mancuso CA, Hickstein DD, Dorney KM, et al. Controlling electron-ion rescattering in two-color circularly polarized femtosecond laser fields. Phys Rev A. 2016;93:053406.
[77] Baykusheva D, Ahsan MS, Lin N, et al. Bicircular high-harmonic spectroscopy reveals dynamical symmetries of atoms and molecules. J Phys Rev Lett. 2016;116:123001.
[78] Liu X, Zhu X, Li L, et al. Selection rules of high-order-harmonic generation: symmetries of molecules and laser fields Phys Rev A. 2016;94:033410.
[79] Mauger F, Bandrauk AD, Uzer TJ. Circularly polarized molecular high harmonic generation using a bicircular laser. Phys B. 2016;49:10LT01.
[80] Reich DM, Madsen LB. Illuminating molecular symmetries with bicircular high-order-harmonic generation. Phys Rev Lett. 2016;117:133902.
[81] Yuan KJ, Bandrauk AD. Attosecond-magnetic-field-pulse generation by electronic currents in bichromatic circularly polarized UV laser fields. Phys Rev A. 2015;92:063401.
[82] Becker W, Chichkov BN, Wellegehausen B. Schemes for the generation of circularly polarized high-order harmonics by two-color mixing. Phys Rev A. 1999;60:1721–1722.
[83] Reich DM, Madsen LB. Rotating-frame perspective on high-order-harmonic generation of circularly polarized light. Phys Rev A. 2016;93:043411.
[84] Bandrauk AD, Lu H. Controlling harmonic generation in molecules with intense laser and static magnetic fields: orientation effects. Phys Rev A. 2003;68:043408.
[85] Zhang L, Xie XH, Roither S, et al. Subcycle control of electron-electron correlation in double ionization. Phys Rev Lett. 2014;112:193002.
[86] Dörner R, Mergel V, Jagutzki O, et al. Cold target recoil ion momentum spectroscopy: a 'momentum microscope' to view atomic collision dynamics. Phys Rep. 2000;330:95–192.
[87] Abel MJ, Pfeifer T, Jullien A, et al. Carrier-envelope phase-dependent quantum interferences in multiphoton ionization. Phys B. 2009;42:075601.
[88] Zille D, Adolph D, Möller M, et al. Chirp and carrier-envelope-phase effects in the multiphoton regime: measurements and analytical modeling of strong-field ionization of sodium. New J Phys. 2018;20:063018.
[89] Kling MF, Rauschenberger J, Verhoef AJ, et al. Imaging of carrier-envelope phase effects in above-threshold ionization with intense few-cycle laser fields. New J Phys. 2008;10:025024–025024–17.
[90] Kling MF, Siedschlag C, Verhoef AJ, et al. Control of electron localization in molecular dissociation. Science. 2006;312:246–248.
[91] Eppink ATJB, Parker DH. Velocity map imaging of ions and electrons using electrostatic lenses: application in photoelectron and photofragment ion imaging of molecular oxygen. Rev Sci Instrum. 1997;68:3477–3484.
[92] Ngoko Djiokap JM, Hu SX, Madsen LB, et al. Electron vortices in photoionization by circularly polarized attosecond pulses. Phys Rev Lett. 2015;115:113004.

[93] Ngoko Djiokap JM, Meremianin AV, Manakov NL, et al. Multistart spiral electron vortices in ionization by circularly polarized UV pulses. Phys Rev A. 2016;94:013408.
[94] Yuan K-J, Chelkowski S, Bandrauk AD. Photoelectron momentum distributions of molecules in bichromatic circularly polarized attosecond UV laser fields. Phys Rev A. 2016;93:053425.
[95] Yuan KJ, Lu HZ, Bandrauk ADJ. Photoionization of triatomic molecular ions by intense bichromatic circularly polarized attosecond UV laser pulses. Phys B. 2017;50:124004.
[96] Li M, Zhang G, Kong X, et al. Phase modulated high density collinear holographic data storage system with phase-retrieval reference beam locking and orthogonal reference encoding. Opt Express. 2018;26:878–886.
[97] Pengel D, Kerbstadt S, Johannmeyer D, et al. Electron vortices in femtosecond multiphoton ionization. Phys Rev Lett. 2017;118:053003.
[98] Pengel D, Kerbstadt S, Englert L, et al. Control of three-dimensional electron vortices from femtosecond multiphoton ionization. Phys Rev A. 2017;96:043426.
[99] Wollenhaupt M, Krug M, Köhler J, et al. Three-dimensional tomographic reconstruction of ultrashort free electron wave packets. Appl Phys B. 2009;95:647–651.
[100] Smeenk C, Arissian L, Staude A, et al. Momentum space tomographic imaging of photoelectrons. J Phys B. 2009;42:185402.
[101] Wollenhaupt M, Lux C, Krug M, et al. Tomographic reconstruction of designer free-electron wave packets. Chem Phys Chem. 2013;14:1341–1349.
[102] Gilb S, Torres EA, Leone SR. Mapping of time-dependent electron orbital alignment. J Phys B. 2006;39:4231.
[103] Bayer T, Gräfing D, Kerbstadt S, et al. Time-resolved 3D imaging of ultrafast spin–orbit wave packet dynamics. New J Phys. 2019;21:033001.
[104] Mauritsson J, Remetter T, Swoboda M, et al. Attosecond electron spectroscopy using a novel interferometric pump-probe technique. Phys Rev Lett. 2010;105:053001.
[105] Remetter T, Johnsson P, Mauritsson J, et al. Attosecond electron wave packet interferometry. Nat Phys. 2006;2:323.
[106] Huismans Y, Rouzée A, Gijsbertsen A, et al. Time-resolved holography with photoelectrons. Science. 2011;331:61–64.
[107] Villeneuve DM, Hockett P, Vrakking MJJ, et al. Coherent imaging of an attosecond electron wave packet. Science. 2017;356:1150.
[108] Lux C, Wollenhaupt M, Bolze T, et al. Circular dichroism in the photoelectron angular distributions of camphor and fenchone from multiphoton ionization with femtosecond laser pulses. Angew Chem Int Ed. 2012;51:5001–5005.
[109] Janssen MHM, Powis I. Detecting chirality in molecules by imaging photoelectron circular dichroism. Phys Chem Chem Phys. 2014;16:856–871.
[110] Dreissigacker I, Lein M. Photoelectron circular dichroism of chiral molecules studied with a continuum-state-corrected strong-field approximation. Phys Rev A. 2014;89:053406.
[111] Beaulieu S, Ferré A, Géneaux R, et al. Universality of photoelectron circular dichroism in the photoionization of chiral molecules. New J Phys. 2016;18:102002.
[112] Ferre A, Handschin C, Dumergue M, et al. A table-top ultrashort light source in the extreme ultraviolet for circular dichroism experiments. Nat Photonics. 2015;9:93–98.
[113] Beaulieu S, Comby A, Clergerie A, et al. Attosecond-resolved photoionization of chiral molecules. Science. 2017;358:1288.
[114] Goulielmakis E, Uiberacker M, Kienberger R, et al. Direct measurement of light waves. Science. 2004;305:1267–1269.

[115] Kienberger R, Goulielmakis E, Uiberacker M, et al. Atomic transient recorder. Nature. 2004;427:817–821.
[116] Eckle P, Smolarski M, Schlup P, et al. Attosecond angular streaking Nat Phys. 2008;4:565–570.
[117] Pfeiffer AN, Cirelli C, Smolarski M, et al. Recent attoclock measurements of strong field ionization. Chem Phys. 2013;414:84–91.
[118] Chang Z, Corkum PB, Leone SR. Attosecond optics and technology: progress to date and future prospects. JOSA B. 2016;33:1081–1097.
[119] Dudovich N, Polack T, Pe'er A, et al. Smearing of phase transition due to a surface effect or a bulk inhomogeneity in ferroelectric nanostructures. Phys Rev Lett. 2005;94:083002 –083002–4.
[120] Bethe HA, Salpeter EE. Quantum mechanics of one- and two-electron atoms. Berlin: Springer; 1957.
[121] Fano U. Propensity rules: an analytical approach. Phys Rev A. 1985;32:617.
[122] Roudnev V, Esry BD. General theory of carrier-envelope phase effects. Phys Rev Lett. 2007;99:220406.
[123] Alnaser AS, Litvinyuk IV. Subfemtosecond directional control of chemical processes in molecules. J Phys B. 2017;50:032002.
[124] Kerbstadt S, Englert L, Bayer T, et al. Ultrashort polarization-tailored bichromatic fields. J Mod Opt. 2017;64:1010.
[125] Kerbstadt S, Timmer D, Englert L, et al. Orthogonal polarization encoding for reduction of interpixel cross talk in holographic data storage. Opt Express. 2017;25:12518.
[126] Lozovoy VV, Pastirk I, Dantus M. Multiphoton intrapulse interference IV ultrashort laser pulse spectral phase characterization and compensation. Opt Lett. 2004;29:1–3.
[127] von Vacano B, Buckup T, Motzkus M. In situ broadband pulse compression for multiphoton microscopy using a shaper-assisted collinear spider. Opt Lett. 2006;31:1154–1156.
[128] Coello Y, Lozovoy VV, Gunaratne TC, et al. Interference without an interferometer: a different approach to measuring, compressing, and shaping ultrashort laser pulses. J Opt Soc Am B. 2008;25:A140–A150.
[129] Galler A, Feurer T. Pulse shaper assisted short laser pulse characterization. Appl Phys B. 2008;90:427–430.
[130] Kak AC, Slaney M. Principles of computerized tomographic imaging. New York, NY: IEEE Press; 1988.
[131] Hockett P, Wollenhaupt M, Lux C, et al. Complete photoionization experiments via ultrafast coherent control with polarization multiplexing. II. Numerics and analysis methodologies. Phys Rev A. 2015;92:013411.
[132] Hockett P, Wollenhaupt M, Baumert T. Coherent control of photoelectron wave-packet angular interferograms. J Phys B. 2015;48:214004.
[133] Wefers MM, Nelson KA. Ultrafast optical waveforms. Science. 1993;262:1381–1382.
[134] Polachek L, Oron D, Silberberg Y. Full control of the spectral polarization of ultra-short pulses. Opt Lett. 2006;31:631–633.
[135] Plewicki M, Weise F, Weber SM, et al. Phase, amplitude, and polarization shaping with a pulse shaper in a Mach-Zehnder interferometer. Appl Opt. 2006;45:8354–8359.
[136] Masihzadeh O, Schlup P, Bartels RA. Improved performance in coaxial holographic data recording. Opt Express. 2007;15:18025–18032.
[137] Ninck M, Galler A, Feurer T, et al. Hydrocarbon-free resonance transition 795-nm rubidium laser. Opt Lett. 2007;32:3379–3381.

[138] Weise F, Lindinger A. Full control over the electric field using four liquid crystal arrays. Opt Lett. 2009;34:1258–12560.
[139] Kupka D, Schlup P, Bartels RA. Simplified ultrafast pulse shaper for tailored polarization states using a birefringent prism. Rev Sci Instrum. 2009;80:053110.
[140] Schwarz C, Huter O, Brixner T. Full vector-field control of ultrashort laser pulses utilizing a single dual-layer spatial light modulator in a common-path setup. JOSA B. 2015;32:933–945.
[141] Rausch S, Binhammer T, Harth A, et al. Few-cycle femtosecond field synthesizer. Opt Express. 2008;16:17410–17419.
[142] Hagemann F, Gause O, Wöste L, et al. Optical fingerprint recognition based on local minutiae structure coding. Opt Express. 2013;21:5536–5549.
[143] Chan H-S, Hsieh Z-M, Liang W-H, et al. Synthesis and measurement of ultrafast waveforms from five discrete optical harmonics. Science. 2011;331:1165.
[144] Baker S, Walmsley IA, Tisch JWG, et al. Femtosecond to attosecond light pulses from a molecular modulator. Nat Phot. 2011;5:664–671.
[145] Schmidt BE, Thiré N, Boivin M, et al. Frequency domain optical parametric amplification Nat Commun. 2014;5:3643.
[146] Yelin D, Meshulach D, Silberberg Y. Adaptive femtosecond pulse compression. Opt Lett. 1997;22:1793–1795.
[147] Shutova M, Zhdanova AA, Sokolov AV. Detection of mixed OAM states via vortex breakup. Phys Lett A. 2017;381:408–412.
[148] Bliokh KY, Ivanov IP, Guzzinati G, et al. Theory and applications of free-electron vortex states. Phys Rep. 2017;690:1–70.
[149] Lloyd SM, Babiker M, Thirunavukkarasu G, et al. Electron vortices: beams with orbital angular momentum. Rev Mod Phys. 2017;89:035004.
[150] Verbeeck J, Tian H, Schattschneider P. Production and application of electron vortex beams. Nature. 2010;467:301–304.
[151] Gariepy G, Leach J, Kim KT, et al. Creating high-harmonic beams with controlled orbital angular momentum. Phys Rev Lett. 2014;113:153901.
[152] Géneaux R, Camper A, Auguste T, et al. Synthesis and characterization of attosecond light vortices in the extreme ultraviolet. Nat Commun. 2016;7.
[153] Gauthier D, Ribič PR, Adhikary G, et al. Tunable orbital angular momentum in high-harmonic generation. Nat Commun. 2017;8:14971.
[154] Dorney KM, Rego L, Brooks NJ, et al. Controlling the polarization and vortex charge of attosecond high-harmonic beams via simultaneous spin–orbit momentum conservation. Nat Phot. 2019;13:123–130.
[155] Paufler W, Böning B, Fritzsche S. Tailored orbital angular momentum in high-order harmonic generation with bicircular Laguerre-Gaussian beams. Phys Rev A. 2018;98:011401.
[156] Hockett P, Wollenhaupt M, Lux C, et al. complete photoionization experiments via ultrafast coherent control with polarization multiplexing. Phys Rev Lett. 2014;112:223001.

Appendix

The model for the description of PMDs from perturbative MPI with a sequence of polarization-controlled bichromatic laser pulses is presented in this appendix. This representation illustrates the close relationship between bichromatic photoionization and nonlinear optical spectroscopy which is established by the multiphoton spectra for the absorption of n_l LCP and

n_r RCP photons. In this picture, the interband N_1- vs. N_2-photon interferences presented in Section 3 are a generalization of the high-order frequency-mixing scheme [73] discussed in Section 2. We start by defining the two laser electric fields $E_\nu(t)$, with $\nu = 1, 2$

$$E_\nu(t) = A_\nu \mathcal{E}_\nu(t)\, e^{i\omega_\nu t} e^{i\varphi_\nu} e^{i\varphi_{ce}}. \tag{11}$$

Herein, A_ν denotes the amplitudes, $\mathcal{E}_\nu(t)$ the envelope functions, ω_ν the center frequencies, φ_ν the relative phases and φ_{ce} a common carrier envelope phase. The shape of the envelope can, for example, be chosen as a Gaussian function

$$\mathcal{E}_\nu(t) = e^{-\left(\frac{t}{\Delta t_\nu}\right)^2} \tag{12}$$

with a pulse duration of Δt_ν, corresponding to a full width at half maximum (FWHM) of $\ln(2)\Delta t_\nu$. A delay of τ is introduced in the second pulse of the sequence. The polarization state of both pulses is taken into account by decomposing both fields into their LCP and RCP components $E_l(t)$ and $E_r(t)$ characterized by the respective coefficients l_ν and r_ν

$$\begin{aligned} E_l(t) &= l_1 E_1(t) + l_2 E_2(t-\tau), \\ E_r(t) &= r_1 E_1(t) + r_2 E_2(t-\tau). \end{aligned} \tag{13}$$

In general, any elliptical polarization state is described by the set of complex valued coefficients. To reproduce the experimental implementation, the coefficients q_ν with $q = l, r$ can be determined by the projections of the vector obtained by applying the Jones matrix of a lambda plate installed under the angle $\mathcal{J}_\Lambda(\alpha_\nu)$ to some initial field polarization e_{in} onto the Jones vectors for LCP (e_l) and RCP (e_r) light

$$q_\nu = \left[\mathcal{J}_\Lambda(\alpha_\nu) e_{in}\right] \cdot e_q. \tag{14}$$

For example, a $\lambda/2$ plate installed under the angle of α results in the coefficients $l = \frac{e^{2i\alpha}}{\sqrt{2}}$ and $r = \frac{e^{-2i\alpha}}{\sqrt{2}}$. The coefficients to describe the pulse sequences discussed in the paper, i.e. CRCP, COCP, OLP and PLP are presented in Table A1.

The nonlinear higher-order temporal field

$$E_{n_l,n_r}(t) = E_l^{n_l}(t) E_r^{n_r}(t) \tag{15}$$

is the quantity which enters the perturbative description of the absorption of n_l LCP photons and n_r RCP photons if no intermediate resonances are present. The corresponding N-photon spectrum for the absorption of $N = n_l + n_r$ photons is the Fourier transform ($\mathcal{F}$) of the higher-order temporal field $E_{n_l,n_r}(t)$ defined in Equation (15)

$$\mathcal{S}_{n_l,n_r}(\omega) = \mathcal{F}\left[\mathbf{E}_{\mathbf{n_l},\mathbf{n_r}}(\mathbf{t})\right](\omega), \tag{16}$$

characterizing the photoelectron kinetic energy distribution $\mathcal{S}_{n_l,n_r}(IP + \hbar\omega)$, where IP is the ionization potential. Assuming ionization by N photons, $N-k$ of which are LCP (k are

Table A1. Coefficients for the CRCP, COPC, OLP and PLP pulse sequences used in the experiments.

	l_1	l_2	r_1	r_2
CRCP	1	0	0	1
COCP	1	1	0	0
OLP	$\frac{1}{\sqrt{2}}$	$\frac{i}{\sqrt{2}}$	$\frac{1}{\sqrt{2}}$	$-\frac{i}{\sqrt{2}}$
PLP	$\frac{1}{\sqrt{2}}$	$\frac{1}{\sqrt{2}}$	$\frac{1}{\sqrt{2}}$	$\frac{1}{\sqrt{2}}$

RCP), the resulting wave function is the product of the energy distribution $\mathcal{S}_{N-k,k}(\omega)$ and the angular distribution $Y_{N,N-2k}(\theta,\phi)$ given by the spherical harmonics

$$\psi_{N,k}(\omega,\theta,\phi) \propto \mathcal{S}_{\boldsymbol{N-k,k}}(\omega)\, Y_{N,N-2k}(\theta,\phi). \tag{17}$$

Hence, the wave function of the angular momentum superposition state created by the absorption of N photons from the bichromatic field reads[2]

$$\psi_N(\omega,\theta,\phi) = i^N \sum_{k=0}^{N} \mathcal{S}_{N-k,k}(\omega)\, w_{N,N-2k}\, Y_{N,N-2k}(\theta,\phi), \tag{18}$$

where $w_{N,N-2k}$ are the sums of products of the Wigner-3j-symbols corresponding to all paths leading to the final state $\psi_{N,k}$. For example, the coefficients relevant for ionization with $N = 3$ and 4 photons are $w_{3,\pm3} = \frac{1}{\sqrt{105}}$, $w_{3,\pm1} = \frac{1}{5\sqrt{7}}$ and $w_{4,\pm4} = \frac{1}{3\sqrt{105}}$, $w_{4,\pm2} = \frac{2}{21\sqrt{15}}$, $w_{4,\pm0} = \frac{2}{35\sqrt{2}}$. The interband interferences presented in Section 3.1 arise from the superposition of states from the absorption of $N_1 \neq N_2$ photons

$$\boldsymbol{\Psi}(\omega,\theta,\phi) = \boldsymbol{\Psi}_{N_1}(\omega,\theta,\phi) + \boldsymbol{\Psi}_{N_2}(\omega,\theta,\phi). \tag{19}$$